Journal of Materials Chemistry A

ROYAL SOCIETY OF CHEMISTRY

REVIEW

View Article Online
View Journal | View Issue

Cite this: J. Mater. Chem. A, 2022, 10, 19211

Carbon nanomaterials–polymer composites for perovskite solar cells: preparation, properties and applications

Qianqian Dou,[a] Tanner Whatley,[a] Tajamul Syed,[b] Wei Wei *[b] and Hui Wang *[ac]

Perovskite solar cells (PSCs) are a rising star in the photovoltaic industry, which achieved an enormous breakthrough in terms of efficiency from an initial 3.8% in 2009 to 25.7% in 2021. The major challenge to bring perovskite solar cells commercially available is the poor long-term device stability. The defects in perovskite and energy loss originating from charge recombination limit the efficiency of perovskite solar cells. Carbon–polymer composites, which feature superb electrical conductivity, outstanding carrier mobility, remarkable flexibility and superior heat and moisture stability, have attracted considerable attention to tackle these issues. With their multifunctional properties, carbon–polymer composites can play various roles in almost every component in the perovskite solar cell architecture. In this review article, recent progress concerning the utilization of carbon–polymer composites in different components in PSCs (*i.e.*, perovskite additives, electrodes, encapsulation layers and charge transport layers) is comprehensively overviewed. Then, future research directions and opportunities toward high-performance perovskite solar cells utilizing carbon–polymer composites are presented.

Received 19th March 2022
Accepted 16th May 2022

DOI: 10.1039/d2ta02175g

rsc.li/materials-a

1. Introduction

Using renewable energy resources (such as solar, wind and geothermal energy) rather than fossil fuels is the key to form a sustainable society and address the global warming issues resulting from the rapid population growth and industrialization.[1–3] Among various renewable resources, solar energy is abundant and environmentally friendly and has immense potential to meet the rising energy demands. Photovoltaic devices that can convert solar energy into electric power are necessary for wider application of solar energy.[4,5] Crystalline silicon solar cells have dominated the photovoltaic (PV) market for decades; however, they suffer from the drawbacks of expensive raw materials and a complicated manufacturing process.

A rising star in the PV industry is hybrid perovskite solar cells (PSCs) that utilize metal halides (*e.g.*, $MAPbX_3$ [$CH_3NH_3PbI_3$]) as the active material. For such PSCs, their power conversion

[a]Department of Mechanical Engineering Department, University of Louisville, 332 Eastern Parkway, Louisville, KY 40292, USA. E-mail: hui.wang.1@louisville.edu
[b]Department of Mechanical Engineering, Wichita State University, 1845 Fairmount Street, Wichita, KS 67260, USA. E-mail: wei.wei@wichita.edu
[c]Conn Center for Renewable Energy Research, University of Louisville, 216 Eastern Parkway, Louisville, KY 40208, USA

Qianqian Dou is a visiting scholar at the University of Louisville. She received her Ph.D. degree in Chemical and Biomolecular Engineering from the Hong Kong University of Science and Technology (HKUST), and then was Postdoctoral fellow at HKUST. Her research mainly focuses on the design and synthesis of nanomaterials for applications in energy conversion and storage, including perovskite solar cells and batteries.

Tanner Whatley is a Graduate Research Assistant in the Mechanical Engineering department at the University of Louisville. He received his bachelor's degree in mechanical engineering at Western Kentucky University. His research mainly focuses on advancements in energy conversion and storage devices, such as perovskite solar cell and batteries.

efficiency (PCE) has experienced skyrocketing rise in the past decade (from 3.8% at 2009 to 25.7% at 2021).[6–10] Recently, the lab-scale efficiency of 25.7% for tin oxide electron transport layer (ETL) based solar cells approached the record efficiency of silicon solar cells.[11] Moreover, a potential efficiency of 31% of lead halide perovskite has been predicted by theoretical simulations.[12] Therefore, high efficiency, cost-effectiveness, easy fabrication and industrial scalability are the advantages of PSCs.[13–16] Nevertheless, one of the biggest challenges for PSCs is the long-term stability to maintain high efficiency, especially when subjected to environmental stresses such as moisture, UV light radiation and heat.[17] There are two negative factors resulting in the performance decay: (1) the photocatalytic degradation of perovskite materials due to the charge transport materials and metal diffusion originating from metal electrodes;[18–20] (2) the ion migration caused by weak Coulomb force in the perovskite lattice.[21,22]

To prevent the performance decay of PSCs, the recombination of electrons and holes within perovskite layers and interfaces should be minimized,[23] and thus carbon nanomaterials with excellent electrical and mechanical properties are highly promising to tackle the bottlenecks of PSCs.[24] For instance, the device with carbon materials (graphene, reduced graphene oxide (rGO), carbon nanotubes (CNTs), *etc.*) as spacer layers, additives or hole transport layers (HTLs) yielded an efficiency greater than 20%.[25–27] Several great reviews have summarized the utilization of carbon materials in PSCs and discussed their properties and roles.[3,5,14,28–31]

Although it is promising to introduce carbon materials into the PSC architecture, it is difficult to directly process a high concertation of them through a surfactant-free solution-based approach.[32] Moreover, two-dimensional carbon materials may cause undesired charge recombination due to the poor contact between layers in the PSC structure.[33] To maximize the advantages, one facile approach is to integrate carbon nanomaterials into a polymer matrix to form composites,[34] which display the synergistic effect between the polymer and nanofillers to achieve improved properties under a wide range of conditions. There have been many reports on nanocomposites that utilize carbon materials (*e.g.*, graphene and its derivatives and carbon nanotubes) in PSC devices; nevertheless, a review that focuses on important discoveries regarding carbon–polymer composites for PSCs is still lacking.

In this review, on the basis of fundamental concepts of PSC structures, we firstly introduced the preparation methods of carbon–polymer nanocomposites, their conductive and mechanical properties and how they are integrated into PSC structures. Then, the state-of-the-art results of using carbon nanomaterials–polymer composites in each component in PSC devices (*e.g.*, perovskite layer, electron/hole transport layer and electrode) are then discussed. Finally, we highlight the prospects for the future development of carbon nanomaterials–polymer composite based PSCs.

2. Working principle and PSC structure

A typical multilayered PSC contains five essential components: (1) a perovskite light absorber layer, (2) an electron transport layer (ETL), (3) a hole transport layer (HTL), (4) a transparent electrode and (5) a back electrode. As shown in Fig. 1a, the general working principle is when exposed to sunlight, photons are captured and electron–hole pairs are generated in the

Tajamul Syed is a graduate research assistant in the Mechanical Engineering Department at Wichita State University. He received his M.S. degree from Wichita State University and his Bachelor of Engineering degree from Osmania University, India. He is currently working on perovskite solar cells.

Dr Wei Wei is an Assistant Professor in Mechanical Engineering Department at Wichita State University. She received her Ph.D. from Michigan Technological University and her B.S. degree from East China University of Science and Technology. Her current research focuses on advanced materials synthesizing, renewable energy conversion devices, photocatalytic processes for H_2 generation, and mechanical properties of composite materials.

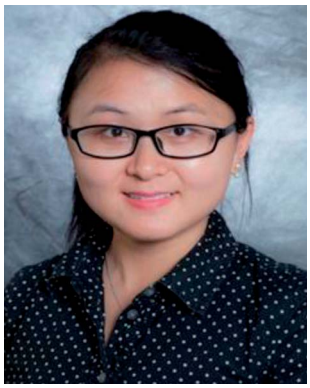

Hui Wang is an Assistant Professor of Mechanical Engineering at the University of Louisville. She received her Ph.D. in Materials Science and Engineering from Michigan Technological University, and then was a Postdoctoral Associate at Oak Ridge National Laboratory. Her research focuses on advanced 762000materials for energy conversion and storage, including carbon materials for solar cells and lithium-/sodium-ion solid conductors for solid-state batteries.

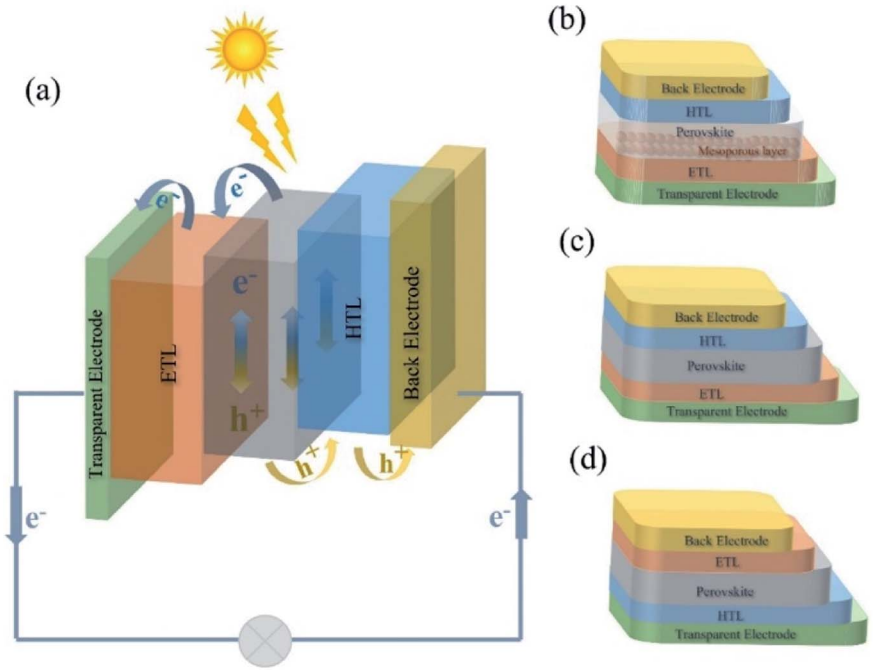

Fig. 1 (a) General working principle of PSCs; device architectures of various PSCs: (b) mesoporous n–i–p, (c) planar n–i–p and (d) inverted p–i–n structured PSCs.

perovskite layer; then electrons move to the ETL and meanwhile holes flow towards the HTL, followed by the electrons and holes extracted to the transparent electrode and a back electrode, respectively. Later, the transparent electrode and back electrode are connected to form an external circuit. The whole process is thermodynamically favorable when the valence and conduction band energy levels of the layers are aligned.[35]

2.1 PSC device architectures

The device architectures for PSCs have undergone tremendous advancement within the last decade.[36] The architecture of PSCs is mainly classified into direct (n–i–p) and inverted (p–i–n) with either a planar or a mesoscopic structure, where n, i, and p stand for donor-type, intrinsic, and acceptor type semiconductors, respectively (Fig. 1b–d). In a planar regular (n–i–p) architecture, the ETL is deposited on transparent conducting glass (transparent electrode), which is followed by depositing the perovskite active layer, and then the HTL is deposited on top of the perovskite film and topped by a metal contact.[23,30] For the mesoporous structure, it refers to the use of a thin and compact titanium oxide (c-TiO_2) layer as a hole blocking layer and a mesoporous TiO_2 or Al_2O_3 (m-TiO_2 or m-Al_2O_3) layer as an electron-extraction scaffold to fill with perovskite materials.[37] In the inverted (p–i–n) configuration, the HTL is a bottom contact below the perovskite layer while the ETL is on the top and contacts with the back electrode (*e.g.*, Al). In general, high-temperature sintering (450 °C) is required for the normal n–i–p and mesoporous structure that commonly employs TiO_2 as an ETL,[38] while the p–i–n structure is more compatible with flexible devices because of its low processing temperatures.[39,40]

2.2 Key components in PSCs

The overall performance of PSCs depends on several factors: the light harvesting separation efficiency of the light absorber layer, charge separation at perovskite/HTL(ETL) interfaces and charge transport in the perovskite, HTL and ETL, respectively.

2.2.1 Electrode. In PSCs, a transparent electrode and back electrode are used to collect the electrons and holes in PSCs, respectively. Transparent conductive oxides such as fluorine doped tin oxide (FTO) and tin doped indium oxide (ITO) are deposited on a glass substrate by a vacuum deposition technique to work as the transparent electrode. Moreover, conductive polymers, metal oxides, carbon nanotubes, graphene, and metals also have been investigated as transparent electrode materials.[41–44] For the back electrode in PSCs, metals (*i.e.*, Au and Ag) and carbon-based materials are the most commonly used materials.[45]

2.2.2 Perovskite-structured materials. Metal halide perovskite adopts the general formula ABX_3, where the A site is a monovalent cation that can be either organic cations MA ($CH_3NH_3^+$), or inorganic Cs^+, K^+, and Rb^+ ions, or their mixture (organic–inorganic hybrid perovskite); B is a divalent metal cation (Pb^{2+} or Sn^{2+}); X represents a halide anion (Cl^-, Br^- or I^-). The A-site cations are related to the band gap and crystal structure stability, while the B site (Pb p orbital) and X site (I p orbital) influence the band edge of perovskites.[28,46] One main challenge that perovskite materials face is their long term stability; for instance, $CH_3NH_3PbI_3$ can degrade into PbI_2 and CH_3NH_3I in the presence of moisture, air and/or UV light.[47]

2.2.3 Charge transport materials. Charge transport materials can be divided into electron transport materials (ETMs) and hole transport materials (HTMs). To ensure high efficiency of devices, they are expected to hold the following features: high

Table 1 Summary and comparison of preparation methods for carbon–polymer composites

Methods	Advantages	Challenges
Solution blending	Simple and commonly used	Requires a large volume of organic solvents and may cause high cost
	Feasible for large scale production	Residual solvents may influence the properties of the composite
In situ polarization	Deals with insoluble and unstable polymers	Difficult to control the level of polymerization
	Strong interaction between carbon materials and polymer	
Melt processing	Environmentally friendly	Hard to form a uniform dispersion
	Thermoplastic polymers	Polymer degradation due to high temperature
Coating	Simple and practical	Layer-by-layer may not homogeneous
	Various choices for coating techniques	

electron (hole) mobility, well-aligned energy levels with the perovskite and electrode, high thermal stability, moisture resistant, and low cost and easy fabrication.

2.2.3.1 Electron transport layer (ETL). The popular inorganic ETL materials include metal oxides such as TiO_2, SnO_2 and ZnO.[48] For such materials, high temperature sintering is typically required to generate an electrically conducting phase (*i.e.*, anatase for TiO_2). Besides, organic ETL materials such as fullerene (C_{60}) and its derivatives (*i.e.* [6,6]-phenyl-C61-butyric acid methyl ester (PCBM)) have been used in inverted PSCs.[49]

2.2.3.2 Hole transport layer (HTL). The commonly used organic HTL materials include spiro-OMeTAD [2,2′,7,7′-tetrakis-(*N*,*N*-di-*p*-methoxyphenylamine)-9,9′-spirobifluorene], P3HT [poly(3-hexylthiophene)], PTAA [poly(triarlyamine)], PANI [polyaniline], PTh [polythiophene], PEDOT [poly(3,4-ethylene dioxythiophene)], PEDOT:PSS [poly(3,4-ethylenedioxythiophene):poly(styrene sulfonate)], *etc.* Taking PEDOT:PSS as an example, it is a polyelectrolyte with hydrophobic PEDOT and hydrophilic PSS and is widely used for inverted PSCs due to its advantages of great transparency in the visible range, high conductivity, and low processing temperature.[50] However, the hygroscopic and acidic nature of PEDOT:PSS may cause the degradation and decomposition of the active layer and ITO electrode, and thus reduce the device stability.[51–53]

Besides, inorganic HTL materials in PSCs include carbonaceous materials (*e.g.* graphene oxide (GO) and reduced graphene oxide (rGO)) due to their good electrical properties, large specific surface area, and outstanding chemical and physical stability.[54–56] However, they also suffer from high oxygen content and poor solvent dispersion, which prevent their wide application.[54,57]

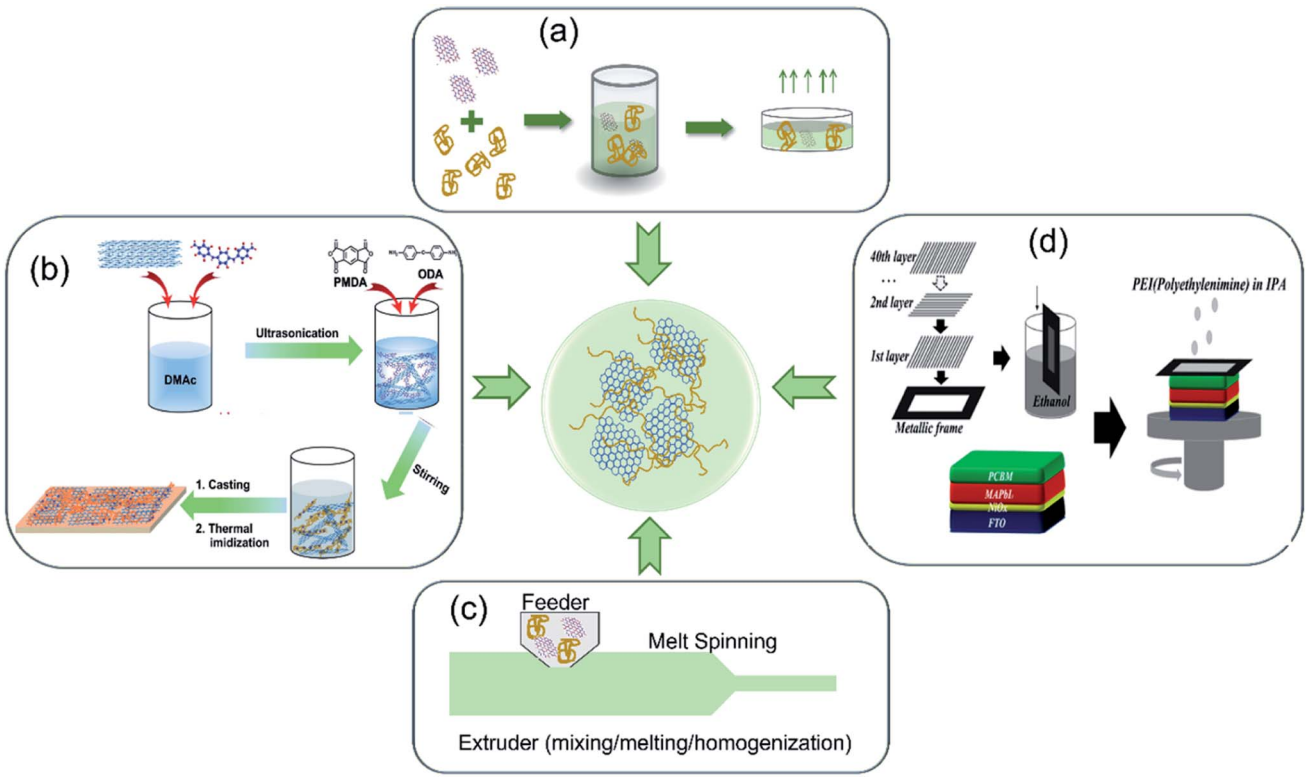

Fig. 2 Preparation methods of carbon nanomaterials–polymer composites: (a) solution blending. (b) *In situ* polymerization. Reproduced with permission.[101] Copyright 2017, Royal Society of Chemistry. (c) Melt processing. Reproduced with permission.[102] Copyright 2020, Elsevier. (d) Coating. Reproduced with permission.[98] Copyright 2018, American Chemical Society.

3. Synthesis of carbon–polymer nanocomposites

Carbon nanomaterials feature the advantages of excellent electrical properties and high stability;[18,58–61] however, the growth of nanostructured carbon sheets in a large area with high quality and their incorporation into PSC devices are difficult and expensive for practical applications. On the other side, polymers are relatively cheap and easy to process, but suffer from high resistance and poor mechanical properties.[62–64] Therefore, the preparation of carbon–polymer nanocomposites is a promising route to achieve synergistic properties, leading to the improvement in the photovoltaic performance of assembled PSCs.[65]

3.1 Carbon materials

Graphene with a 2D layer structure, first synthesized by Andre Geim and Konstantin Novoselov in 2004,[66] is considered as the building block for all carbon structure with other dimensionalities. It possesses good optical transparency ($\approx$97.7%),[67] a high Young's modulus ($\approx$1 TPa),[68] remarkable carrier mobility at room temperature ($\approx$200 000 $cm^2\ V^{-1}\ s^{-1}$),[69] excellent thermal conductivity ($\approx 5 \times 103\ W\ m^{-1}\ K^{-1}$),[70] and superior environmental stability.[71] Regarding its application in PSCs, one main challenge is to obtain uniform and thin graphene films.[72] Graphene oxide (GO), the most popular graphene derivative, is a single layer of graphene nanosheets functionalized with epoxy, carbonyl and hydroxyl groups.[54,73] These functional groups enable GO to disperse easily in water, but also result in its poor electronic conductivity. Reduced graphene oxide (rGO) that hold fewer functional groups than GO have exhibited improvement in electronic characteristics.[74,75]

Carbon nanotubes (CNTs), 1D cylindrical carbon allotropes of graphene, discovered by Sumio Iijima,[76] include single walled nanotubes (SWNTs) from a rolled single graphene sheet, and multi-walled nanotubes (MWNTs) from the stacking of concentric layers of several graphene layers.[77]

Carbon dots are considered as a kind of zero dimensional (0D) carbon dominated nanomaterial with sizes less than 10 nm.[78] Since the first report of carbon dots in 2004, their superior properties such as tunable photoluminescence, low toxicity and light stability have favored their wide application.[79] The abundant functional groups of carbon dots endow them with prospects for modification application in perovskite solar cells and perovskite LEDs.[80–82] Carbon dots include graphene quantum dots (GQDs), carbon quantum dots (CQDs), carbon nanodots (CNDs), carbonized polymer dots,[78,83] *etc.*

3.2 Preparation methods of carbon–polymer nanocomposites

So far, most polymer–carbon nanocomposites have been prepared through methods of (1) solution blending, (2) *in situ* polymerization, (3) melt mixing, and (4) coating. Other approaches include electrospinning, electro-deposition, *etc*. For each method, the detailed preparation process and examples are described as below, and their features are summarized and compared in Table 1.

3.2.1 Solution blending. Solution blending is the simplest method for nanocomposite preparation. In this method (Fig. 2a), carbon nanomaterials and polymers are separately dispersed in a suitable solvent (water or organic) and then mixed; later, the solution mixture is coated on a substrate, followed by evaporation to remove the solvent. For the solvent blending method, one critical step is to obtain the homogeneous dispersion of carbon nanomaterials in the polymer, achieving strong interaction and adhesion between them. To prevent the self-aggregation of graphene or carbon nanotubes, it is important to carefully select appropriate solvents to dissolve the host polymer and carbon nanomaterials.[65] For examples, Han *et al.* chose chlorobenzene (C_6H_5Cl) to disperse PMMA [poly(methyl methacrylate)] and rGO, and then sonicated the mixture;[84] Zheng *et al.* prepared a compact CNTs–P3HT film *via* dispersing them in C_6H_5Cl, followed by sonification and stirring.[85] For some water-soluble polymers such as PEDOT:PSS, deionized (DI) water is used as the solvent to dissolve the polymer and graphene oxide (GO) either directly adding GO powder into PEDOT:PSS aqueous solution[86] or mixing GO in water dispersion with PEDOT:PSS solution.[51]

In addition to the solvent selection, other facile approaches to facilitate the formation of homogeneous mixture solution include: (1) the modification of carbon nanostructures and (2) the functionalization of polymers. In the first way, it involves grafting polymer chains on the surface of carbon nanomaterials to establish strong chemical bonds between them.[87] For instance, Gatti *et al.* attached PhOMe [*p*-methoxyphenyl] substituents to SWCNT and rGO, respectively,[88] to help their good dispersion in P3HT matrix (3 wt% SWCNT∼PhOMe in P3HT and 4 wt% rGO∼PhOMe in P3HT composites). The homogeneous composites promoted the formation of efficient charge percolation pathways in HTL layer. In the second way, functionalizing polymers helps to form a homogeneous mixing and facilitate a good interaction. Jung *et al.* employed PSSA [poly(styrenesulfonic acid)] as a polymer template for solubilizing and stabilizing PANI in water,[89] and then mixed PSSA–PANI aqueous solution with GO dispersion to prepare a graphene–PANI nanocomposite suspension, which was observed to be stable for several weeks without precipitation.

Solution blending is one of the most effective and simple methods to prepare homogeneous composites and also easy to scale-up. Since it uses organic solvents to disperse carbon materials and polymers, the solution blending method requires a drying process to remove solvents. Organic solvents may increase the cost of this method and also possibly affect the composite performance if they are not removed completely.[90]

3.2.2 *In situ* polymerization. For the *in situ* polymerization strategy (Fig. 2b), carbon nanomaterials are mixed with monomers (or pre-polymers) in a selective solvent, and then the curing agent is added to initiate the polymerization reaction. Since monomers are used rather than polymers as the starting materials, the *in situ* polymerization process leads to carbon–polymer nanocomposites with more uniform compositions and stronger interaction.

There are two approaches to initiate the polymer formation process: a chemical way or physical method. For example, in the chemical polymerization of PANI, an oxidative agent also as the curing agent is required. Ammonium persulfate [$(NH_4)_2S_2O_8$, APS] in HCl solution was dropwise added to the mixture of rGO and aniline [$C_6H_5NH_2$] in DI water, producing a rGO–PANI composite;[91] potassium persulfate [$K_2S_2O_8$, KPS] also caused the polymerization of anilines along the basal planes of rGO to form rGO–PANI nanocomposites.[92] In addition, a physical method (such as plasma treatment) can also initiate the polymer formation. Cogal *et al.* reported the use of RF-plasma to prepare a PEDOT/PTh–graphene composite, in which graphene powder was spread into the plasma chamber and exposed to plasma produced by the RF generator; meanwhile the monomer vapors flowed through the chamber, leading to polymer formation on the surface of graphene nanosheets.[93] In this method, the polymer coating's thickness can be controlled by tuning the deposition time of RF-plasma.

In situ polymerization is a great choice to deal with insoluble and unstable polymers. This technique also leads to a strong interaction between carbon materials and polymers. However, it is challenging to use this method to fully control the polymerization level and achieve high levels of exfoliation in large-scale production.

3.2.3 Melt processing. In this method (Fig. 2c), thermoplastic polymers are heated to a molten state, and then mixed and blended with carbon nanomaterials, followed by extrusion to produce nanocomposites. The popular thermoplastic polymers include PP [polypropylene], PS [polystyrene], PC [polycarbonate], PEN [poly(ethylene-2,6-naphthalate)], *etc.*[94,95] Shen *et al.* mixed PC and rGO in chloroform (C_6H_5Cl) solution, followed by stirring, sonication and centrifugation to collect the precipitation, and then the dried composite was melt-mixed at 240 °C in a lab extruder to produce rGO–PC composites that contain PC wrapped on the surface of rGO with noncovalent π–π stacking interaction.[96] The melt-mixing approach is more efficient than the traditional mixing for the dispersion of dry graphene nanoparticles in polymers.[97]

Compared to the two previous methods, melt processing is less versatile and more environmentally friendly to form carbon–polymer nanocomposites, and thus is favorable for commercial production. But this method usually deals with thermoplastic polymers. And the uniform dispersion of carbon materials is hindered due to the high viscosity of thermoplastic polymers. Additionally, high temperature processing may also cause polymer degradation.

3.2.4 Coating. The coating method involves three different ways: (1) directly immersing polymers into the solution of carbon nanomaterials, (2) layer-by-layer spin-coating of a carbon film and polymer film, and (3) the mixed way (immersion and spin coating) (Fig. 2d). In the direct immersion way, the porous structure of CNTs facilitated the infiltration of PEI [polyethylenimine], resulting in a uniform cross-stacked CNT–PEI composite.[98] Using the layer-by-layer strategy, GO solution in chlorobenzene and PMMA in chlorobenzene were each sequentially spin-coated on a SWNT film, followed by drying and annealing to from a SWNT–GO–PMMA composite.[99] In addition, a graphene–Ag nanowire (AgNW)–polymer hybrid composite was reported through the mixed immersion plus spin-coating way, whereas AgNW solution was firstly spin-coated onto a clean graphene–PTFE substrate, and then the polymer in chloroform solution was coated onto the PTFE–graphene–AgNW structure, followed by an annealing process to ensure an integral composite.[100]

The coating methods such as spin-coating, spray-coating, roll-to-roll, and other coating techniques (lab- or large-scale) are feasible and practical to prepare carbon–polymer composite films. Although these methods often require subsequent drying/sintering and pressing treatment, they are appropriate to produce thin films and coatings.

3.3 Physical and chemical properties of polymer–carbon nanocomposites

The nanocomposites that contain both carbon materials and polymers display impressive physical and chemical properties, including conductivity and thermal and mechanical properties.[103]

3.3.1 Conductivity. High conductivity is important to achieve great photovoltaic properties of PSCs. Since carbon materials hold great electrical conductivity, adding them into polymers is expected to significantly improve their conductivity due to the formed electron transport networks.[104] For example, a rGO–PS composite displayed an electrical conductivity enhancement by five orders of magnitude upon increasing the rGO concentration from 0.25 vol% to 2.5 vol%;[105] a GO–PANI composite also exhibited an improved conductivity of 10 S cm^{-1} and specific capacitance of 531 F g^{-1} as compared to 2 S cm^{-1} and 216 F g^{-1} of pure PANI.[106] Mabrouk *et al.* compared the conductivity of three polymers (PEDOT:PSS, PANI, and PANI–PEDOT:PSS) and their composite films with GO, and found that the PANI–PEDOT:PSS–GO composite exhibited the highest conductivity of 0.814 S cm^{-1} owing to the synergistic effect and better interaction between each component.[107]

Besides the electrical conductivity, the hole mobility of composite interlayers in PSCs was also improved. For instance, a GO doped PEDOT:PSS HTL film showed a hole mobility of 1.57 $\times 10^{-4}$ cm^2 V^{-1} s^{-1}, about one order of magnitude higher than the value of pristine PEDOT:PSS (5.55×10^{-5} cm^2 V^{-1} s^{-1}).[51]

3.3.2 Thermal properties. Improving thermal conductivity in PSCs can effectively reduce the thermal damage of perovskite and sprio-OMeTAD materials and thus improve the long-term stability. For polymer–carbon nanocomposites, the thermal conductivity is influenced by many factors, such as the composition, the preparation technique and the geometry distribution of the carbon material in the polymer matrix.[108,109] For example, Yu *et al.* observed that the thermal conductivity of a 25 vol% graphene–epoxy composite was 6.44 W mK^{-1}, which is ~30 times higher than the value of pristine epoxy (0.201 W mK^{-1}).[110] More so, Guo *et al.* reported that a 25 wt% graphene–epoxy composite showed an improved thermal conductivity of 2.67 W mK^{-1}.[111] In another case, 10 vol% multilayer graphene–epoxy nanocomposites displayed an increased thermal

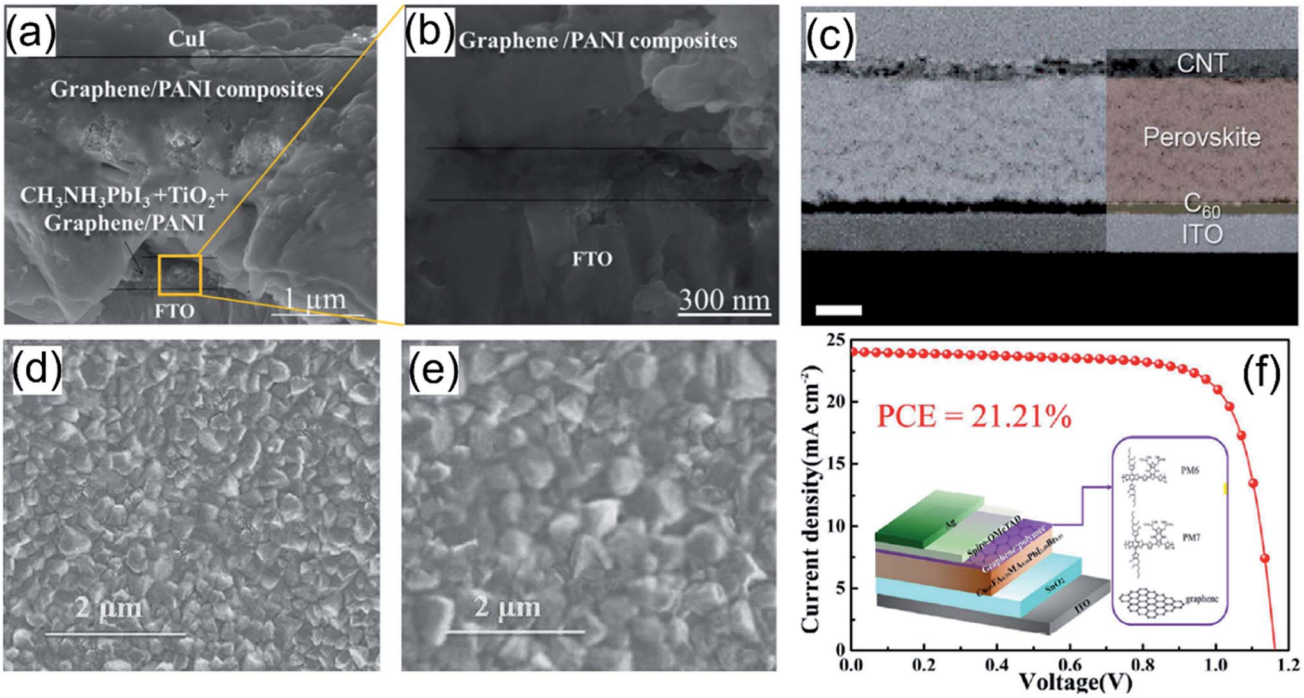

Fig. 3 (a) and (b) Cross-sectional scanning electron microscopy image of the graphene/PANI protected $CH_3NH_3PbI_3$ solar cell. Reproduced with permission.[117] Copyright 2016, Institute of Physics Publishing. (c) Cross-sectional SEM images of the ITO/C_{60}/MAPbI$_3$/CNT device with a carbon-sandwich structure. Reproduced with permission.[118] Copyright 2018, Royal Society of Chemistry. (d) FSEM images of $CH_3NH_3PbI_3$ and (e) FSEM images of perovskite + rGO–P3HT. Reproduced with permission.[120] Copyright 2019, Elsevier. (f) Device architecture and *J*–*V* curve for the best devices of PSCs based on graphene/PM6. Reproduced with permission.[123] Copyright 2021, American Chemical Society.

conductivity of 5.1 W mK^{-1}, which is 23 times higher than the initial value of epoxy.[112]

A difference between the inside temperature and ambient temperature of a solar cell module can be as large as 45 °C when it is exposed to sunlight at 100 mW cm^{-2} irradiance.[113] Materials with good thermal conductivity and thermal stability are desired for solar cells. Giuri *et al.* used DSC and TGA to analyze the thermal behavior of a PEDOT:PSS–GO composite and found that the thermal stability of polymer materials was enhanced when GO was added.[86] Besides, the carbon–polymer composite also showed good thermal conductivity. Due to fast heat dissipation through the thermally conductive rGO–PMMA composite, the thermal stability of the PSC device with such a composite film as the encapsulation layer was found to improve.[84] The PCE of the device with rGO–PMMA coating was about 80% of initial value after 100 h at 85 °C. Meanwhile the efficiency of bare PSC and PMMA coated PSCs decreased by 50% and 60% in 96 h at 85 °C. The thermally conductive rGO–PMMA coating minimized the thermal damage of PSC devices.

3.3.3 Mechanical properties. Carbon–polymer nanocomposites are also reported to show the enhancement of the mechanical properties (*i.e.* elastic modulus, friction coefficient, modulus, and flexibility) due to interface interlocking.[114] Qian *et al.* reported that 1 wt% MWNT–PS composites exhibited an elastic modulus of 1690 MPa and a strength of 16 MPa, which were increased by 42% and ~25% in comparison with bare PS, respectively.[115] Zhao *et al.* loaded CNTs into a hydroxyapatite composite and reported a friction coefficient decrease as well as wear resistance increase.[116] For flexible optoelectronic devices, the graphene–polymer composites contribute to the mechanical robustness against repeated bending. Dong *et al.* prepared a graphene–Ag nanowires–polymer composite and evaluated its flexibility by a bending test with a radius of curvature of 2.0 mm.[100] After 250 cycles of tensile folding, the resistance only increased by 8% without any visible cracking or tearing on the surface.

4. Applications of carbon–polymer nanocomposites in PSCs

Carbon nanomaterials such as graphene and carbon nanotubes are incorporated with polymers to form carbon–polymer nanocomposites. These materials have played different roles in PSCs, including as additives in the perovskite layer, electrodes, electron transporters, hole transporters, barrier layers, *etc.* The PSCs that contain carbon–polymer materials show enhanced performance including higher PCE values and long-term stability. In PSCs, the use of carbon–polymer materials contributes to one or more of the following aspects: (1) high quality perovskite films with high crystallinity and fewer defects; (2) improving conductivity to facilitate charge extraction and transportation; (3) adjustment of the work function between different layers to achieve higher open circuit voltage; (4) great interface contact between layers to enable rapid carrier transport; (5) changing the hydrophobicity and thermal properties to prevent the attack from moisture and heat.

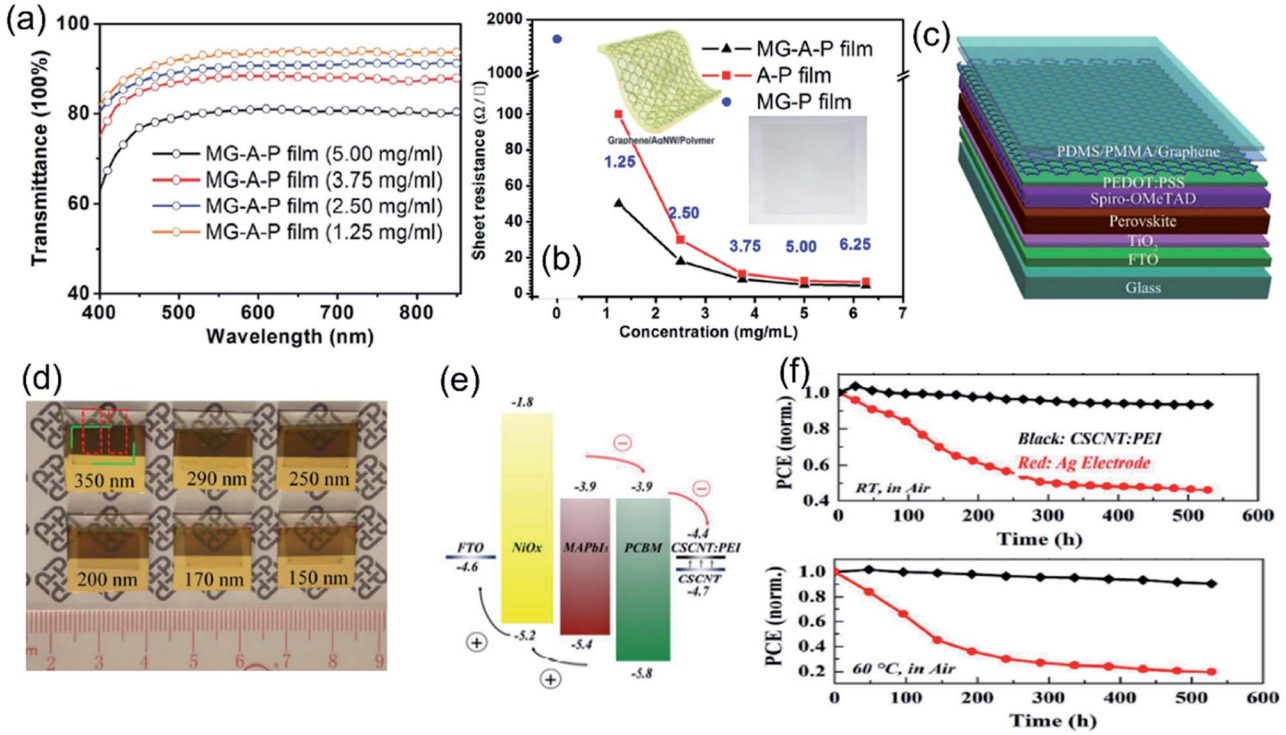

Fig. 4 (a) Optical transmittance spectra of the graphene–AgNWs–polymer (MG–A–P) film with various concentrations of AgNWs and (b) sheet resistance of the MG–P, MG–A–P, and A–P hybrid films with different concentrations of AgNWs. Reproduced with permission.[100] Copyright 2016, American Chemical Society. (c) Schematic diagram of a semitransparent perovskite solar cell using graphene as the counter electrode and (d) photos of semitransparent perovskite solar cells with transparent graphene electrodes. The thicknesses of the perovskite layers in the six devices are approximately 350, 290, 200, 170, and 150 nm, respectively. Reproduced with permission.[58] Copyright 2015, Wiley-VCH. (e) Schematic energy level diagram of the FTO/NiO_x/$MAPbI_3$/PCBM/CSCNT:PEI device and (f) the variation of the PCE of Ag and CSCNT:PEI based PSCs as a function of ageing time at room temperature (RH: 10–50% and T: 20–30 °C) and with a constant temperature of 60 °C. Reproduced with permission.[98] Copyright 2018, American Chemical Society.

4.1 Additives in the perovskite active layer

In the perovskite layer, carbon–polymer nanocomposites can play the following roles: (1) protective coating on the surface of perovskite and (2) an additive in the perovskite layer.

First, a protective coating on the perovskite surface is to prevent its degradation in working environments (air and humid). Rajamanickam *et al.* reported the deposition of a graphene–PANI composite on the top of a $CH_3NH_3PbI_3$ layer to protect it from degradation.[117] The morphology image (Fig. 3a and b) showed that the perovskite crystals were fully encapsulated by the graphene–PANI composite rather than exposed to ambient conditions in the cases of graphene nanosheets- and PANI-only. The assembled PSCs were exposed for 96 h to extremely high humidity (99% RH), and no perovskite degradation was observed. Moreover, a thick graphene–PANI composite coating (~4 μm) increased the tortuosity for water molecules and oxygen diffusion into the perovskite material. In addition, Ahn *et al.* designed a carbon-sandwiched PSC structure (Fig. 3c, C_{60}/$MAPbI_3$/SWCNT), in which a lead halide perovskite layer was sandwiched by C_{60} and SWCNTs without metal electrodes.[118] The PSC devices with three HTMs (spiro-MeOTAD, PTAA and P3HT) incorporated in SWCNTs gave an average PCE of 17.0%, 15.3% and 13.6%, respectively. The supramolecular CNT–polymer hybrids were formed by inducing π–π interactions between polymers and CNTs;[119] specifically, P3HT led to a much better stability than PTAA due to its planar conformation, which led to a close interaction with CNTs by wrapping around nanotubes.

Second, additives are used to influence the crystallization and growth of perovskites or reduce defects in perovskite materials during operation. Sarvari *et al.* grafted reduced graphene oxide with P3HT (or PTEt) and added the rGO–P3HT composite (or rGO–PTEt) into the perovskite precursor solution.[120] The composite additives effectively enhanced the grain size and increased the crystallinity (Fig. 3d and e), and thus improved the absorbance efficiency of pristine perovskite due to grafting of the rGO surface with the polymeric backbones. The P3HT–rGO-based PSC device showed a PCE of 15.15% with a V_{oc} of 0.95 V, a J_{sc} of 22.15 mA cm^{-2}, and an FF of 72%. In addition, for working PSC devices, some harmful defects (*i.e.* local positive and negative ion vacancies) are formed as the cation and halogen ions of perovskite migrate under the internal electric field of the device.[121,122] Recently, Lou *et al.* added a graphene–polymer (*e.g.* PM6, PM7 Lewis base conductive polymer) nanocomposite during the antisolvent step of Cs/FA/MA [$Cs_{0.05}$-$FA_{0.79}MA_{0.16}PbI_{2.49}Br_{0.51}$].[123] The highly conductive graphene–polymer composites not only passivated the defects dominated

by state traps, but also facilitated the charge transport in the perovskite film, which reduced the interfacial charge density and trap-assisted charge recombination. The PSCs with a graphene–PM6 composite additive showed a high PCE of 21.21% (Fig. 3f) with a V_{oc} of 1.17 V, a J_{sc} of 24.03 mA cm^{-2}, and an FF of 76%, compared to the PCE (18.21%) of the control device without the composite. Moreover, due to the hydrophobicity of polymer–graphene composites, the graphene–PM6 and graphene–PM7-based devices showed outstanding stability by maintaining 90% and 85% of the initial PCE after 480 h aging under ~35% RH at room temperature, respectively.

4.2 Electrode

4.2.1 Transparent electrode. Carbon–polymer thin films, with good flexibility and transparency, have shown promise as a transparent electrode for solar cells. Dong *et al.* employed up–bottom preparation to produce a flat hybrid electrode of graphene–Ag nanowire–polymer (MG–A–P), which exhibited better optical–electrical properties (sheet resistance 8.06 Ω □$^{-1}$ and 88.3% optical transmittance at 550 nm as shown in Fig. 4a and b) than the traditional transparent electrode such as ITO.[100] Moreover, the resistance of the MG–A–P hybrid film increased 8% after 250 cycles of the bending test with a radius of curvature of 2.0 mm, while the ITO–PET film rapidly cracked, and the resistance remarkably increased after 5 cycles of the bending test. The enhanced properties result from the hybrid structure, in which the polymer matrix entirely wrapped the conductive components (graphene and Ag wire). Due to the excellent mechanical properties, carbon–polymer based materials possess tremendous potential in application for flexible PSCs that feature high efficiency, low cost and light weight.[124] However, as a transparent electrode, carbon–polymer thin films need to balance the conductivity and light transparency. A higher carbon content in the composite results in higher conductivity but leads to poor light transparency.

4.2.2 Back electrode. Metallic materials such as gold and silver which have high conductivity are typically used back electrodes in PSCs. However, their high temperature vacuum evaporation deposition increase the fabrication cost.[125] The migration of metals to the perovskite layer severely compromise the long-term stability of devices.[20,126] Carbon–polymer nanocomposites are demonstrated as great candidates to replace metal electrodes because of their low cost, flexibility, good conductivity and chemical inertness. You *et al.* reported semi-transparent PSC devices that utilize a graphene–PMMA–PDMS [polydimethylsiloxane] film with PEDOT:PSS spin-coated on the graphene surface (Fig. 4c).[58] The PEDOT:PSS layer introduced more holes in the graphene film and improved the conductivity, with sheet resistance decreased from 1050 Ω sq.$^{-1}$ to 260 Ω sq.$^{-1}$. The obtained PSC devices had a transparency of 50% for the 150 nm thick perovskite layer (Fig. 4d). Thus, the PSC devices showed an average PCE of up to 12.02% and 11.65% from bottom (FTO side) and top (graphene side) electrode illumination, respectively. In addition, Zhou *et al.* demonstrated a cross-stacked carbon nanotube (CSCNT)–PEI (0.5 wt%) composite electrode for inverted PSCs.[98] The presence of PEI promoted a better interface contact and charge transfer between the HTL (PCBM) and CSCNT electrode, and also tuned

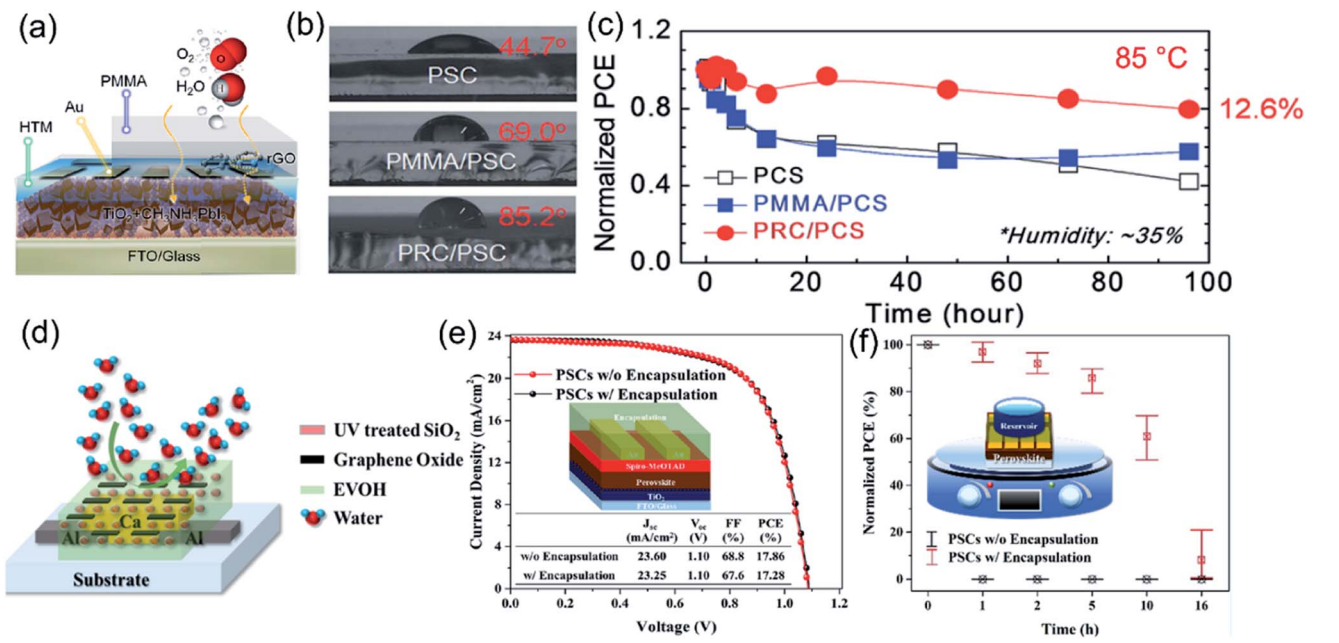

Fig. 5 (a) Schematic representation of the hydrophobic surface and external matter following a complex path through the PRC layer, (b) water contact angles of bare cells, PMMA/PSC and PRC/PSC on the top, and (c) change in the PCE of PSCs at 85 °C for 96 h (normalized using the PCEs of the as-fabricated cells). Reproduced with permission.[84] Copyright 2017, Royal Society of Chemistry. (d) Scheme of PSCs encapsulated with EVOH/S5/UV/G1, (e) efficiency of PSCs before and after encapsulation, and (f) reservoir test of PSCs encapsulated with EVOH/S5/UV/G1. Reproduced with permission.[127] Copyright 2019, American Chemical Society.

Table 2 Summary of the device configurations and PV performances of PSCs using carbon–polymer composites as additives, electrodes and encapsulation layers

Role	Composite materials	Perovskite	Electrode/ETL	HTL/electrode	PCE (%)	J_{sc} (mA)	V_{oc} (V)	FF (%)	Stability	Ref.
Additive in the perovskite layer	Graphene–PANI	$CH_3NH_3PbI_3$	FTO/TiO_2	CuI/Au	—	—	—	—	<10% decrease, 96 h, 99% RH	117
	rGO–P3HT	$CH_3NH_3PbI_3$	FTO/b-TiO_2/mp-TiO_2	Spiro-OMeTAD/MoO_3/Ag	15.1	22	0.95	72	N/A	120
	Graphene–PM7	$Cs0.05FA_{0.79}MA_{0.16}PbI_{2.49}Br_{0.5}$	ITO/SnO_2	Spiro-OMeTAD/Ag	21.2	24	1.16	76	10% decrease, 480 h, 35% RH	123
	CNT–PTAA	$CH_3NH_3PbI_3$	ITO/C_{60}	CNT–PTAA	15.3	23	0.98	67	N/A	118
Electrode	Graphene–PEDOT:PSS	$CH_3NH_3PbI_{3x}Cl_x$	FTO/TiO_2	Spiro-OMeTAD/PEDOT:PSS–graphene	12.3	19	0.96	67	N/A	58
	MG–A–P	$CH_3NH_3PbI_3$	Ag/BCP/PCBM	MoO_3/MG–A–P	10.4	—	—	—	N/A	100
	CSCNT–PEI	$MAPbI_3$	CSCNT–PEI/PCBM	NiO_x/FTO	10.8	18	0.95	61	94% remained after 500 h	98
	CNT–P3HT	$CH_3NH_3PbI_3$	FTO/c-TiO_2/m-TiO_2	CNT–P3HT	13.4	22	0.91	65	97% remained after 40 days	85
Encapsulation layer	rGO–PMMA	$CH_3NH_3PbI_3$	FTO/mp-TiO_2	Spiro-OMeTAD/Au	15.7	22	1.01	0.68	100% remained after 1000 h in air	84
	EVOH–GO–SiO_2	$CH_3NH_3PbI_3$	FTO/TiO_2	Spiro-OMeTAD/Au	17.3	23	1.1	67	86% remained after 5 h in contact with water	127

the work function of the electrode in the inverted PSC (Fig. 4e), yielding a PCE of ~11% for the assembled PSCs. Moreover, since the CSCNT–PEI electrode was thermotolerant without metal-ion diffusion and accumulation, the resultant PSCs showed an increase in stability, and specifically, they retained over 94% of original efficiencies after 500 h storage in ambient air and 90% after 500 h thermal treatment at 60 °C (Fig. 4f). Similarly, Zheng *et al.* developed mesoscopic PSCs using P3HT modified CNTs (CNTs@P3HT) as the counter electrode.[85] In the P3HT–CNT composite, P3HT not only tightly bound the CNTs together to form a cross-linked structure to improve the interaction with the perovskite layer and enable rapid carrier transport, but also extracted holes to facilitate carrier separation due to its hole-transporting properties.

Carbon–polymer composites, as back electrode candidates, show the advantages of (1) easy to process to thin films with tunable thickness and components as well as properties; (2) low cost and excellent mechanical properties; (3) great stability towards perovskite structures. However, the conductivity of the composites is relatively lower than that of metal electrodes especially when insulating polymers are added. Thus, the combination of metal and transparent conductive oxide electrodes leads to high efficiency of PSC devices.

4.3 Encapsulation layer

CNMs–polymer composite coatings also function as a barrier layer, which significantly increases the long-term stability of PSCs in humid and hot environments. Han *et al.* deposited a PMMA–rGO composite (PRC) passivation layer on the top surface of PSCs (Fig. 5a).[84] The rGO nanosheets with hydroxyl groups and amphiphilic PMMA molecules with carbonyl groups contributed to the hydrophobic nature (Fig. 5b) and better thermal conductivity of the PMMA–rGO composite coating, improving the photovoltaic stability under humid environment and high-temperature conditions. With the PMMA–rGO passivation layer, the PSC devices displayed a slight decrease of 10% of the PCE after exposure to very humid conditions (RH > 75%) for 500 hours. When exposed to 90 °C for 100 hours, the PCE of PSC devices with the passivation layer was maintained at 12.6%, which is about 80% of the initial value (Fig. 5c). Jang *et al.* reported an encapsulation layer consisting of GO and SiO_2 fillers in the EVOH [poly(vinyl alcohol-*co*-ethylene)] matrix (Fig. 5d).[127] SiO_2 nanoparticles (5 wt%) were added into EVOH to reduce the permeation of oxygen and water and introducing 1 wt% GO into EVOH/SiO_2 further decreased the water vapor transmission rate (WVTR). The EVOH–GO–SiO_2 encapsulation layer did not damage the efficiency of PSC devices, which showed a PCE of 17.86% with and 17.28% without the layer (Fig. 5e). Moreover, with the composite protective layer, the PSC devices retained approximately 86% and 61% of the initial PCEs after 5 and 10 h from the onset of the reservoir test (direct contact with water on the encapsulated surface). In comparison, the unencapsulated device was immediately degraded after contacting with water (Fig. 5f). Table 2 summaries the device configurations and PV performances of PSCs using carbon–polymer composites as additives, electrodes and encapsulation layers.

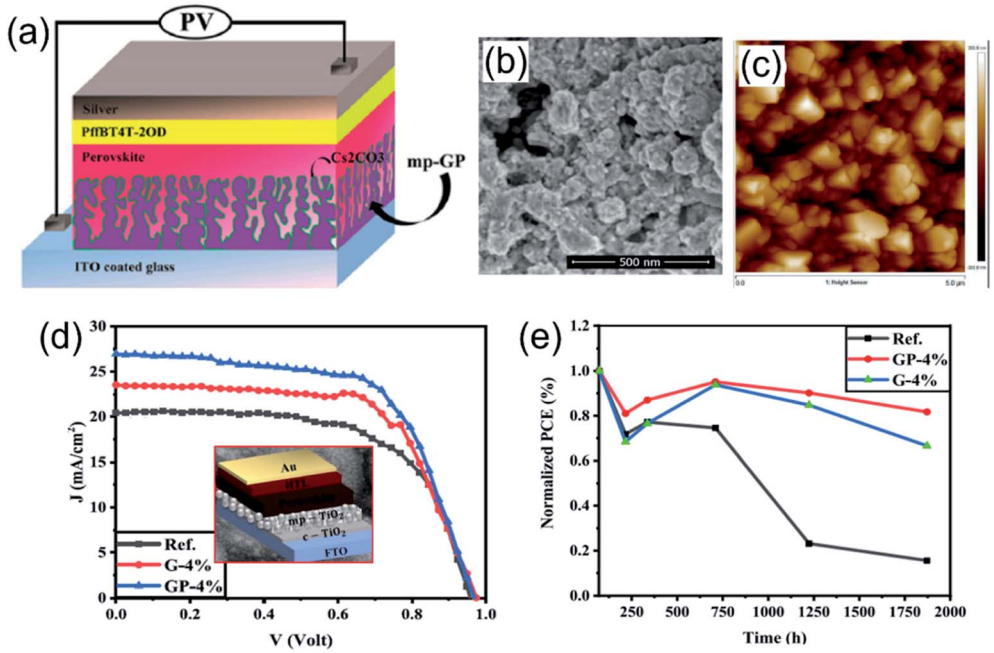

Fig. 6 (a) Schematic view of the device structure with ITO/mp-GP or rGO/Cs_2CO_3/$CH_3NH_3PbI_3$/PffBT4T-2OD/Ag, and (b) SEM image and (c) AFM image of the topography of the mp-GP thin films. Reproduced with permission.[92] Copyright 2016, American Chemical Society. (d) The *J*–*V* of the perovskite solar cells (PSCs) fabricated based on pure mp-TiO_2 and the mp-TiO_2 ETL modified with the rGO–PANI nanocomposite or pure rGO, and (e) stability test of different perovskite solar cells inside a dry airbox with a relative humidity of about 20% in the dark at room temperature. Reproduced with permission.[91] Copyright 2021, Elsevier.

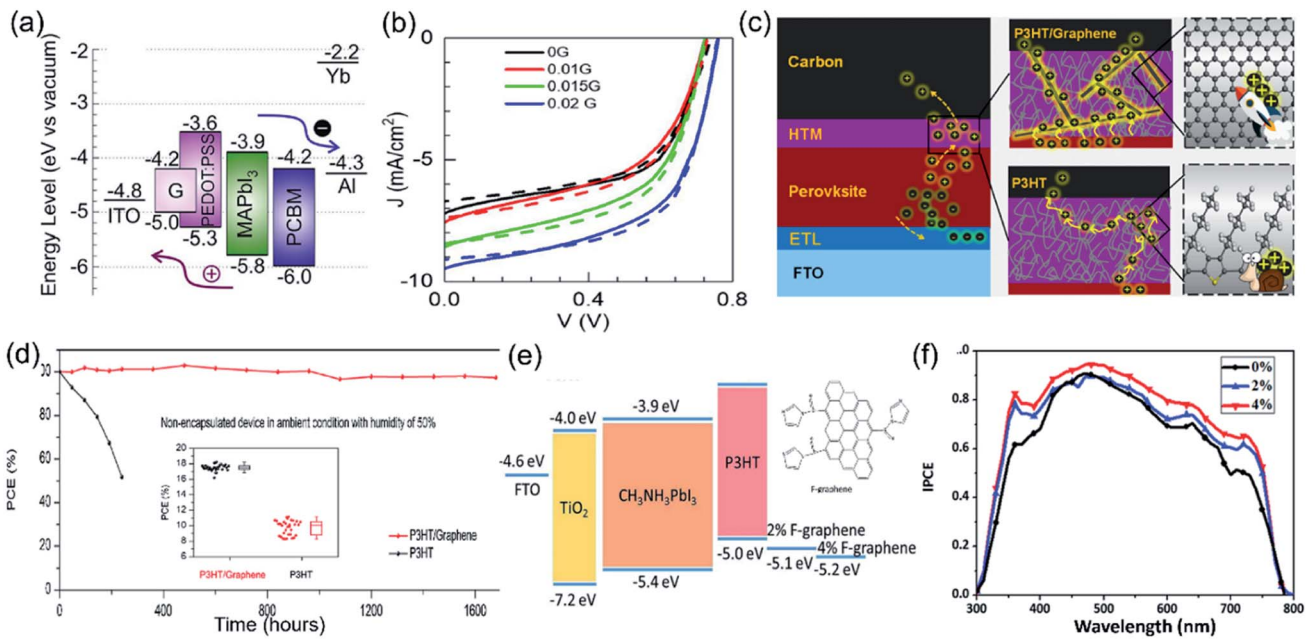

Fig. 7 (a) Energy level diagram for a PSC with graphene-doped PEDOT:PSS as the HTL material, (b) current–voltage performances under 1 sun illumination for the solar cells based on 0G, 0.005G, 0.01G, 0.015G and 0.02G as HTLs in forward sweep (solid lines) and reverse sweep (dashed lines). Reproduced with permission.[132] Copyright 2020, Elsevier. (c) Illustration of a device with P3HT as the HTL, where the hole transport is slow, resulting in charge accumulation, and a device with the P3HT–graphene composite HTL, where holes are transported to the carbon electrode quickly, and (d) normalized PCE evolution of non-encapsulated devices with P3HT and graphene–P3HT as the HTLs stored in the dark for 1680 h in air; the inset shows the statistical PCEs of devices with graphene–P3HT and P3HT as HTLs. Reproduced with permission.[133] Copyright 2019, Elsevier. (e) The schematic energy diagram of the hole-transporting layer involved in the PSCs and (f) the corresponding external quantum efficiency (EQE) spectra of the PSC devices with various HTMs. Reproduced with permission.[134] Copyright 2016, Royal Society of Chemistry.

4.4 Charge transport layer

Carbon nanomaterials–polymer composites are proven to be good candidates for both ETL and HTL materials in PSC structures. In the composite, the combination of polymer (amorphous nature and strong intrachain charge transfer along the conjugated backbone) and carbon nanomaterials with great conductivity enables their good balance between high film quality and charge mobility.

4.4.1 Electron transport layer (ETL). PANI is a popular polymer that has been widely used together with carbon nanomaterials in ETLs.[128,129] The carbon–PANI nanocomposite can either serve as a promising ETL material or function as an additive.

In 2016, Tong *et al.* demonstrated the use of mesoporous graphene–PANI (mp-GP) as a ETL candidate in PSC devices (Fig. 6a) with good thermal stability.[92] The network structure of the mp-GP composite contains pores (100–400 nm), which not only form well-connected fast electronic channels but also allow for the formation of larger perovskite crystals (Fig. 6b and c). The resultant mp-GP based PSC device displayed a remarkable PCE of 13.8% in comparison to 9.3% of the rGO based device. Regarding the stability, it is known that the basicity of ETL materials (*e.g.* ZnO) is one driving force for the thermal decomposition of perovskite.[130] Mp-GP with a low isoelectric point strengthened the stability of perovskite better against thermal decomposition. Moreover, the mesoporous architecture protected the inner perovskite grains from moisture attack and reactive interface formation. For mp-GP based devices, their PCE remained at ~88% of initial efficiency after 200 h thermal annealing at 150 °C. This mesoporous graphene–polymer composite served as a promising ETL material.

Recently, Mohseni *et al.* added a rGO–PANI nanocomposite as an additive to a typical mesoporous TiO_2 (mp-TiO_2) ETL precursor in mesoscopic-type PSCs, leading to the reduction in surface defects and passivated grain boundaries of the upper perovskite layer.[91] Furthermore, the incorporation of the rGO–PANI nanocomposite strengthened the charge transfer in the ETL layer as well as the interface with the perovskite. The 4 vol% rGO–PANI-based device achieved the highest PCE of 16.48% (Fig. 6d) and also displayed enhanced stability, whereas 82% of initial PCE was maintained over an aging time of 1870 h inside a dry airbox at a temperature of 20–30 °C (Fig. 6e). In contrast, the PCE of the rGO-based device declined to 15% of its original value.

4.4.2 Hole transport layer (HTL). Typically, PSC devices contain organic spiro-OMeTAD as the HTL material. Alternative materials include PEDOT:PSS and P3HT. PEDOT:PSS is a popular polymer that combines with graphene and related materials (GO and rGO) to form composites. The work function of PEDOT–DOT is 5.08 eV, which well-matches with graphene

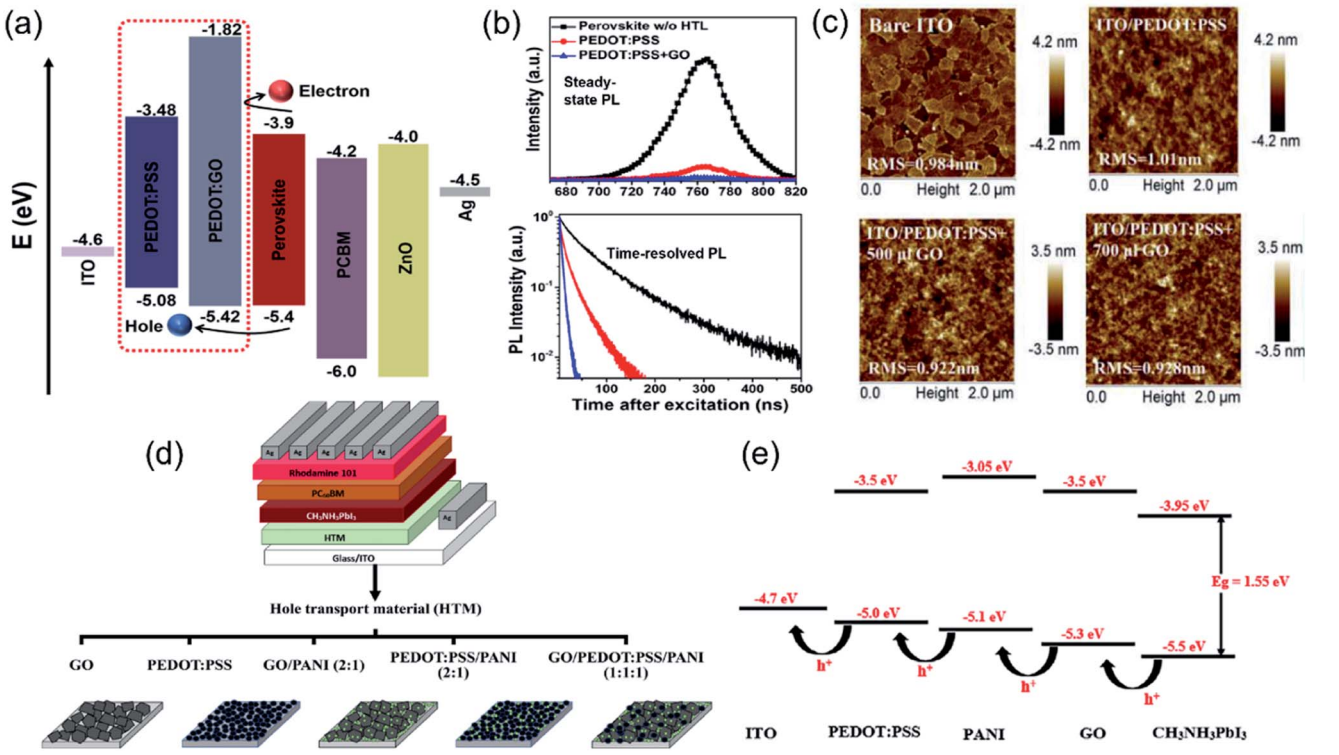

Fig. 8 (a) Relative energy levels of the various device components in the perovskite solar cells, (b) steady-state PL spectra and time-resolved PL spectra of perovskite films prepared on PEDOT:PSS and GO–PEDOT:PSS composites, respectively. Reproduced with permission.[135] Copyright 2018, Springer Nature. (c) AFM images of GO-doped PEDOT:PSS films spin-coated on ITO glass using different concentrations. Reproduced with permission.[51] Copyright 2017, Elsevier. (d) Structure of p–i–n perovskite solar cells using different HTMs:GO, PEDOT:PSS, GO–PANI, PEDOT:PSS–PANI, and GO–PEDOT:PSS–PANI nanocomposites, and (e) schematic diagram showing the energy levels of ITO, $CH_3NH_3PbI_3$ perovskite and different HTMs, including PEDOT:PSS, PANI, and GO. Reproduced with permission.[107] Copyright 2020, Wiley-VCH.

oxide (4.9 eV) and results in more efficient charge transport and collection at the electrode.[131]

To take advantage of the high conductivity and hydrophobicity of pristine graphene, nanocomposites of graphene–polymers have been explored using various polymers such as PEDOT, PEDOT:PSS, and P3HT. In 2018, Cogal *et al.* reported the preparation of nanocomposites of graphene with PTh [polythiophene] or PEDOT prepared using radio frequency (RF) plasma polymerization.[93] They found that the PSC devices with I_2 doped PEDOT–graphene showed higher PCE (8.79%) than I_2 doped PTh–graphene (4.95%). Later, Redondo-Obispo *et al.* reported the incorporation of few-layer graphene platelets into PEDOT:PSS (Fig. 7a) to form a HTL composite, which influenced the subsequent growth of the perovskite layer (*i.e.* inhibited the formation of PbI_2 and decreased grain boundary density).[132] The G-doped PEDOT:PSS composite also exhibited better charge extraction and reduction of recombination at the interface between the composite HTL and perovskite. The PSC device with a 0.02 mg mL^{-1} G-doped PEDOT:PSS HTL displayed the highest PCE (Fig. 7b). In 2019, Chu *et al.* developed a P3HT–graphene composite to replace pure P3HT as the HTL material in PSC devices (Fig. 7c).[133] The graphene–P3HT composite exhibited an outstanding hole mobility of 1.2×10^{-2} cm^2 V^{-1} s^{-1}, two orders of magnitude larger than that of pure P3HT. The carbon-based PSC with the graphene–P3HT composite achieved a high PCE of 18.1% in comparison to 11.1% of the pure P3HT-based PSC. Impressively, the devices with the graphene–P3HT composite HTL showed long-term stability, which was revealed by 97% remained PCE after storage for 1680 hours under ambient conditions (RH 50%) without illumination (Fig. 7d). In addition to pristine graphene, a functional graphene (F-graphene)-modified P3HT composite has been prepared by Ye *et al.* and employed as a HTL in PSC devices. The high conductivity of F-graphene enhanced the hole mobility of the composite HTL and modified the energy level of the device (Fig. 7e).[134] Using 4 wt% F-graphene in the P3HT layer, the PSCs with the composite HTL showed the highest EQE value and IPCE value (Fig. 7f), consistent with the highest PCE of 13.82%.

Graphene oxide (GO) has been used to form composites with polymers including PEDOT:PSS, PEDOT, and PANI. In 2016, Lee *et al.* investigated a GO–PEDOT:PSS composite as the HTL for planar PSCs, and they observed higher photovoltaic performance of PSCs with the composite HTL (9.74%) than those of pristine PEDOT:PSS (8.23%) and GO (6.42%) HTLs.[131] The enhanced performance is attributed to more efficient hole transport and collection. In 2018, Yu *et al.* fabricated inverted PSCs through the solution-mixing method to prepare a GO–PEDOT:PSS composite as the HTL.[135] The GO–PEDOT:PSS (volume ratio of 2 to 1) composite showed a better matched HOMO level (5.42 eV) with that of the perovskite layer (5.4 eV)

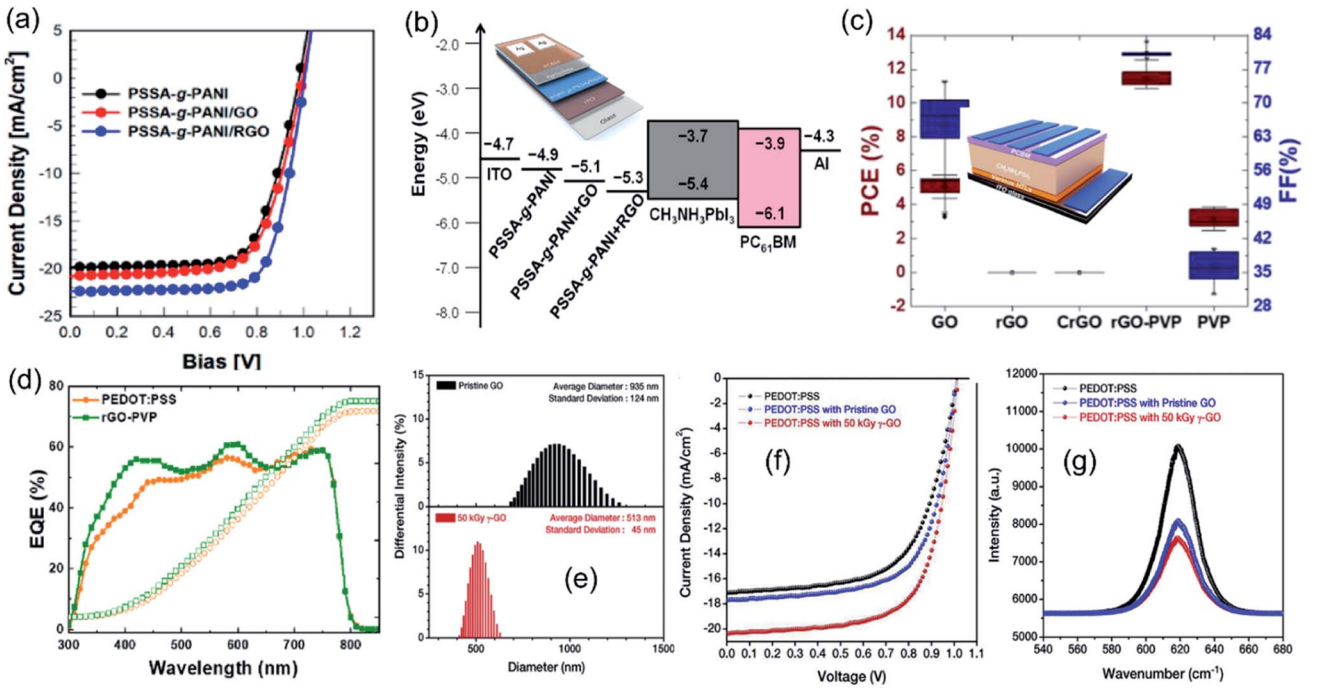

Fig. 9 (a) *J–V* curves of PSCs with PANI, GO–PANI, and rGO–PANI as HTLs under 1-sun illumination and (b) energy levels of composite films in PSCs (inset shows the schematic device structure). Reproduced with permission.[89] Copyright 2021, Multidisciplinary Digital Publishing Institute. (c) Statistical data of the PCE and FF of PSCs with various HTLs (inset shows the schematic of the rGO–PVP-based PSC device structure) and (d) EQEs with the integrated J_{sc} of PSCs using PEDOT:PSS and rGO–PVP as HTLs. Reproduced with permission.[137] Copyright 2021, Elsevier. (e) Size distributions of pristine GO and 50 kGy γ-ray-GO dispersed in water measured by DLS measurements, (f) *J–V* curves and EQE spectra of the cells with PEDOT:PSS, PEDOT:PSS with pristine GO, and PEDOT:PSS with 50 kGy γ-ray-GO as hole transport layers, and (g) photoluminescence spectra of perovskite layers on the PEDOT:PSS layer, PEDOT:PSS with GO, and with 50 kGy γ-ray-GO. Reproduced with permission.[138] Copyright 2018, Elsevier.

than pristine PEDOT:PSS (5.08 eV) (Fig. 8a), improving the hole extraction. The inverted PSC with the composite HTL displayed a PCE of 18.09%, higher than that of the PSC with pristine PEDOT:PSS (14.95%). The steady-state and time-resolved photoluminescence (PL) spectra (Fig. 8b) also confirmed that the PL intensity of the perovskite film prepared on the PEDOT:GO composite decreased about 97%, along with a remarkably decreased exciton lifetime. With the GO–PEDOT:PSS composite HTL, Niu *et al.* studied the influence of different concentrations of GO on the photostatic performance of PSC devices.[51] The GO doping into PEDOT:PSS reduced the root mean square (RMS) roughness value (Fig. 8c) and provided a high quality surface for perovskite deposition. They observed that the PSC with PEDOT:PSS + 500 μL GO showed the highest J_{sc} value (20 mA cm^{-2}) and PCE (14.2%) since the oversaturated GO in composites caused segregation and barriers between GO and PEDOT:PSS as well as poor conductivity. In addition, Mabrouk *et al.* compared five different HTL materials for p–i–n PSCs: pristine GO, PEDOT:PSS, PEDOT:PSS–PANI (2/1), GO–PANI (2/1), and PANI–PEDOT:PSS–GO (1 : 1 : 1) (Fig. 8d).[107] When using the GO–PEDOT:PSS–PANI (ratio of 1 : 1 : 1) composite as the HTL, the PSC device achieved the highest efficiency of 18.12%. The enhanced J_{sc} value was attributed to the higher conductivity and well-matched energy levels (Fig. 8e); meanwhile, the improved V_{oc} resulted from the increase of the work function after adding GO to PEDOT:PSS–PANI. The surface chemistry of GO can be functionalized with atomic groups and form composites with polymers. Guo *et al.* prepared sulfated

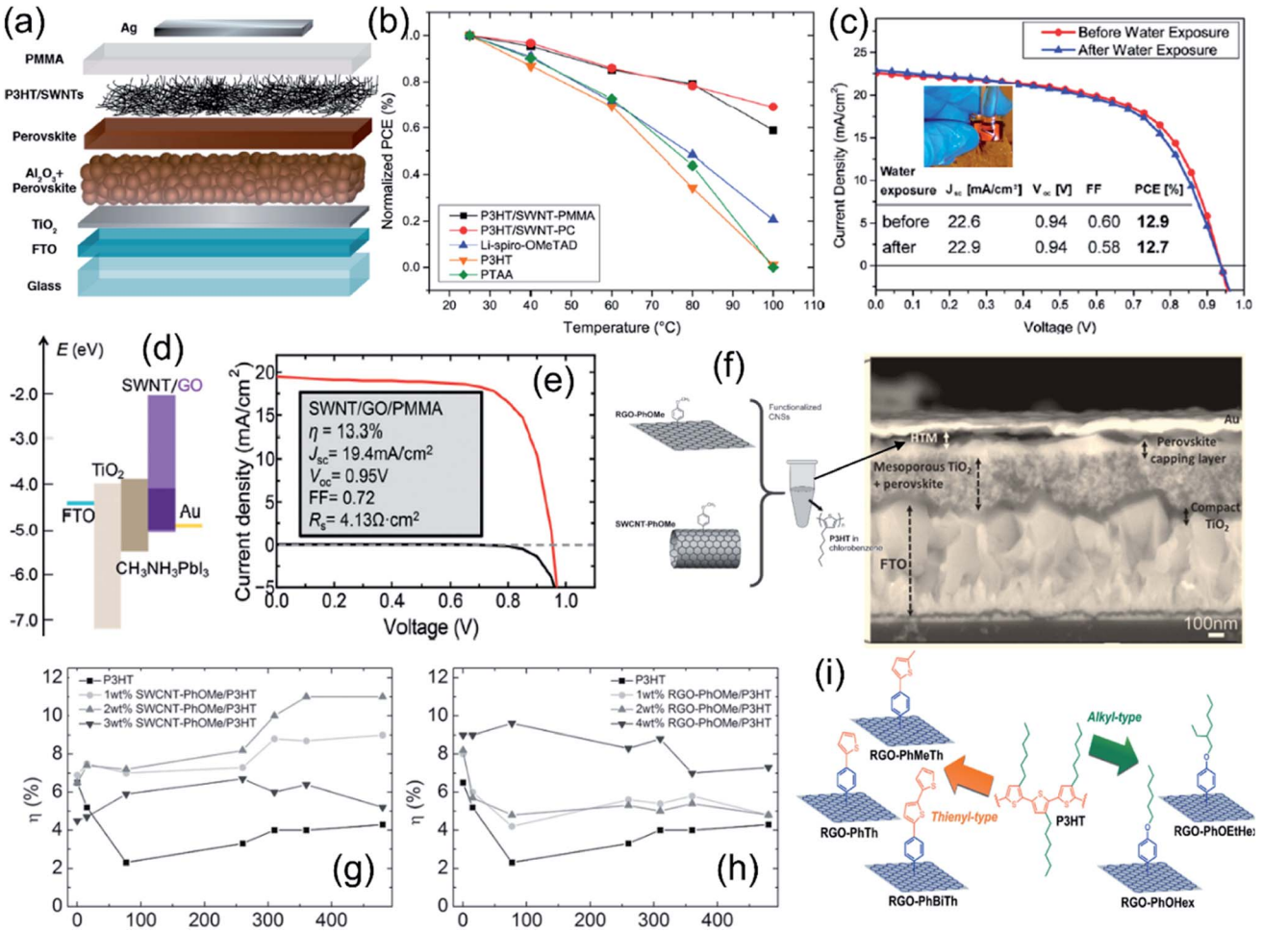

Fig. 10 (a) Schematic illustration of the solar cell with a carbon nanotube–polymer composite as the hole-transporting structure, (b) power conversion efficiency of perovskite solar cells employing a range of hole-extraction layers as a function of temperature, and (c) current density–voltage plots recorded under AM1.5 simulated sunlight of 100 mW cm^{-2} irradiance of a complete perovskite solar cell employing a SWNT–P3HT–PC hole-extraction layer before and after being placed under running water for 60 s; the inset shows a photograph of the same perovskite solar cell placed under a flowing tap with the active layer on top. Reproduced with permission.[17] Copyright 2014, American Chemical Society. (d) Band alignment in a perovskite/SWNT/GO solar cell and (e) *J*–*V* curve of a perovskite solar cell using SWNT–GO–PMMA as the HTL under light (red solid line) and in the dark (black solid line). Reproduced with permission.[99] Copyright 2016, Royal Society of Chemistry. (f) Left: *p*-methoxyphenyl functionalized carbon nanostructure–P3HT blend and right: cross-sectional SEM images of a perovskite solar cell with a 1 wt% rGO–PhOMe–P3HT blend HTM, (g) endurance tests for devices based on SWCNT–PhOMe–P3HT blends, and (h) endurance tests for devices based on rGO–PhOMe–P3HT blends used as HTMs. Reproduced with permission.[88] Copyright 2016, Wiley-VCH. (i) Schematic illustration of the five types of functionalized rGO species reported in ref. Reproduced with permission.[144] Copyright 2018, Wiley-VCH.

Table 3 Summary of the device configurations and PV performances of PSCs using carbon–polymer composites as charge transport layers

Role	Composite materials	Perovskite	Electrode/ETL	HTL/electrode	PCE (%)	J_{sc} (mA)	V_{oc} (V)	FF (%)	Stability	Ref.
HTL	Graphene doped PEDOT:PSS	$MAPbI_3$	ITO/PCBM	Graphene doped PEDOT:PSS/Al	—	—	—	—	N/A	132
	Graphene–P3HT	$FA_{0.3}MA_{0.7}PbI_3$	FTO/SnO_2@TiO_2	Graphene–P3HT/carbon	18.1	22	1.09	74	97% remained after 600 h	133
	F-Graphene doped P3HT	$CH_3NH_3PbI_3$	FTO/TiO_2	F-Graphene–P3HT/Ag	13.8	19	0.99	71	70% remained after 8 weeks	134
	GO–PEDOT:PSS	$CH_3NH_3PbI_3$	Ag/PCBM	GO–PEDOT:PSS/ITO	9.74	15	0.84	73	Stable up to 48 h	131
	GO doped PEDOT:PSS	$CH_3NH_3PbI_3$	Ag/PCBM	GO–PEDOT:PSS/ITO	14.2	20	0.9	79	N/A	51
	sGO–PEDOT:PSS	$CH_3NH_3PbI_3$	Ag/PCBM	sGO–PEDOT:PSS/ITO	13.9	19	1.0	67	N/A	136
	GO–PEDOT:PSS	$CH_3NH_3PbI_3$	Ag/PCBM	GO–PEDOT:PSS/ITO	18.1	21	1.02	82	80% remained after 25 days	135
	γ-Ray-GO–PEDOT:PSS	$CH_3NH_3PbI_3$	Al/PCBM	γ-Ray-GO–PEDOT:PSS/ITO	12.7	18	1.0	74	N/A	138
	GO–PEDOT:PSS–PANI	$CH_3NH_3PbI_3$	Ag/PCBM	GO–PEDOT:PSS–PANI/ITO	18.1	23	1.05	75	25% remained after 80 days	107
	SWCNT–PhOMe–P3HT	$CH_3NH_3PbI_3$	FTO/TiO_2	SWCNT–PhOMe–P3HT/Au	11.6	22	0.62	85	8.7% remained after a 3240 h endurance test	88
	rGO–PhOMe–P3HT	$CH_3NH_3PbI_3$	FTO/TiO_2	rGO–PhOMe/P3HT/Au	10	19	0.62	86	4.7% remained after a 3240 h endurance test	88
	Functionalized rGO–P3HT	$Cs_{0.15}FA_{0.8}5PbI_3$	FTO/C_{60}	Functionalized rGO–P3HT/Au	9.8	—	—	—	N/A	144
	I_2 doped PEDOT–graphene	$(FAPbI_3)_{0.85}(MAPbBr_3)_{0.15}$	FTO/TiO_2	I_2 doped PEDOT–graphene/Au	8.79	21	0.79	52	72% remained after 180 days	93
	rGO–PVP	$CH_3NH_3PbI_3$	Au/PCBM	rGO–PVP/ITO	11.36	15	0.97	80	50% remained after 1000 h	137
	rGO–PANI	$CH_3NH_3PbI_3$	Ag/BCP/PCBM	rGO–PANI/ITO	16.6	22	1.0	74	87% retained after 500 h	89
	GQDs–PEDOT:PSS	$CH_3NH_3PbI_3$	Ag/PCBM	GQDs–PEDOT:PSS/FTO	15.24	21	0.995	71	77% remained after 9 days	139
	CNDs–PEDOT:PSS	$CH_3NH_3PbI_3$	Ag/PCBM + BCP	CNDs–PEDOT:PSS/ITO	18.03	22.6	1.01	79	70% remained after 60 days	140
	SWNT–GO–PMMA	$CH_3NH_3PbI_3$	FTO/c-TiO_2/m-TiO_2	SWNT–GO–PMMA/Au	13.3	19	0.95	72	98% remained after 10 days, 70–80% RH	99
	SWNT–P3HT–PMMA	$CH_3NH_3PbI_3$	FTO/TiO_2/Al_2O_3	SWNT–P3HT–PMMA/Ag	15.3	23	1.02	66	∼10% drop at 80 °C in 96 h	17
	SWNT–P3HT	$CH_3NH_3PbI_3$	FTO/TiO_2	SWNT–P3HT/spiro-OMeTAD/Ag	15.4	21	1.02	71	N/A	141
	SWNT–P3HT	$FA_{0.83}MA_{0.17}Pb(I_{0.87}Br_{0.17})_3$	FTO/SnO_2	SWNT–P3HT/spiro-OMeTAD/Ag	18.8	22	1.14	75	N/A	142
	MWCNT–P3HT	$CsPbI_2Br$	FTO/TiO_2/	MWCNT–P3HT/carbon	10.0	13	1.21	62	85% remained after 250 h	143
ETL	rGO–PANI	$CsMAFAPbI_3$	FTO/mp-TiO_2 + rGO–PANI	Spiro-OMeTAD/Au	16.5	26	0.96	63	82% remained after 1870 h	91
	mp-GP	$CH_3NH_3PbI_3$	ITO/mp-GP/Cs_2CO_3	PffBT4T-2OD/Ag	13.8	—	—	—	88% remained after 200 h	92

graphene oxide (sGO) with $-SO_3H$ groups and combined it with PEDOT:PSS to form composites as HTLs for PSCs.[136] They found that sGO as a HTL showed better device efficiencies (max. PCE 9.9%) than the GO HTL (max. PCE 6.7%). Moreover, the 1 : 1 sGO–PEDOT composite HTL based device achieved the best PCE of 13.9% and less photocurrent hysteresis due to the most efficient charge carrier generation and transfer.

Reduced graphene oxide (rGO) as another 2D graphene derivative has been explored to prepare carbon–polymer composites for HTL materials. Jung *et al.* prepared rGO–PANI nanocomposite films and demonstrated them as HTL materials in inverted PSCs.[89] The rGO–PANI based device achieved a PCE of 16.61%, higher than that of PSCs with GO–PANI as the HTL (14.1%) (Fig. 9a). The enhanced photostatic performance was attributed to the higher conductivity and better energy level matching to the perovskite layer with the rGO–PANI nanocomposite (Fig. 9b). Recently, Cho *et al.* used an electron beam to reduce a GO–PVP composite in aqueous ethanol solution and prepared a highly dispersible rGO–PVP nanocomposite.[137] PVP acted as a stabilizer to impede the re-aggregation during the reduction process of GO. When used as a HTL in PSCs, the aggregation-free rGO–PVP nanocomposite showed the highest PCE of 11.36% (Fig. 9c) and more efficient photon-to-electron conversion than other HTL materials (GO, PVP, and PEDOT:PSS) (Fig. 9d). To obtain better dispersion in polymer, Cho *et al.* employed high energy ^{60}Co γ-ray irradiation to produce smaller GO sheets (Fig. 9e) and uniform distribution of γ-ray irradiated GO in PEDOT:PSS.[138] The better dispersion resulted in more efficient hole charge transport between GO and PEDOT:PSS in the HTL. The γ-ray-GO embedded PEDOT:PSS interlayer assisted in improving the crystallinity of the perovskite layer, resulting in a higher photovoltaic performance with a PCE of 12.76% than the devices without GO or with pristine GO (Fig. 9f). Moreover, the photoluminescence spectra (Fig. 9g) also confirmed the best charge separation in the PSCs with a γ-ray-GO–PEDOT:PSS composite.

Carbon dots usually have various functional groups such as carbonyl, hydroxyl, and epoxy groups.[82] The interaction between carbon dots and PEDOT:PSS can enhance the conductivity of the composite. Li *et al.* incorporated graphene quantum dots (GQDs) into PEDOT:PSS and used this composite film as a HTL.[139] They found that GQDs increased the conductivity of the composite film because graphene quantum dots interacted with the PEDOT:PSS chain, leading to phase separation. The average PCE was boosted from 12.77% for PEDOT:PSS based PSCs to 15.24% for PEDOT:PSS–GQD based devices. Li *et al.* developed a S, C co-doped carbon nanodots (CNDs)–PEDOT:PSS composite HTL for inverted PSCs.[140] The sulfur double bond of functionalized CNDs banded the superfluous PSS and removed the insulating component from the PEDOT:PSS mixture, resulting in conductivity and hole extraction capability enhancement. Meanwhile, the amidogen on the surface of functionalized CNDs neutralized hydrogen ions from PSS and lowered the level of acidity of PEDOT:PSS. The optimized PSCs demonstrated a promising air stability and photovoltaic performance including a V_{oc} of 1.01 V, a J_{sc} of 22.6 mA cm^{-2}, and a FF 79.06%, yielding a PCE of 18.03%.

Polymer-functionalized single walled carbon nanotubes (SWNTs) have been employed to work as a HTL material. In 2014, Habisreutinger *et al.* wrapped P3HT with SWNTs to form a supramolecular nanohybrid film by spin-coating and combined it with insulating PMMA to prepare meso-superstructured PSCs (Fig. 10a).[17] The P3HT–SWNT–PMMA based PSCs displayed a maximum PCE of 15.3% and impressive thermal stability, where the average scanned PCE before and after thermal stressing at 80 °C for 96 h changed from 11.1 to 10.1%. In addition, the PSC device on SWNT–P3HT–PC showed improved thermal stability at temperature above 80 °C (Fig. 10b) as well as moisture stability by the comparison of an unsealed device before and after exposure to running water (Fig. 10c). The composite of functionalized SWNTs within the inert polymer matrix achieved competitive efficiency and offered resilience against thermal and moisture stressing. The authors also deposited spiro-OMeTAD on the P3HT–SWNT layer.[141] Spiro-OMeTAD filled the opening and gaps of the nanotube layer, which facilitated an efficient charge transfer. The device with a stratified structure of P3HT–SWNT and Spiro-OMeTAD yielded a PCE of 15.4%. In 2017, Habisreutinger *et al.* further demonstrated a PCE of 18.8% for the device with a double-layer structure of P3HT–SWNT and spiro-OMeTAD as a hole-transporting p-type layer and $FA_{0.83}MA_{0.17}Pb(I_{0.87}Br_{0.17})_3$ as an absorber.[142] Besides, Wang *et al.* reported the use of a SWNT–GO–PMMA thin film as a hole conductive protecting layer in PSCs.[99] In the composite, GO acts as an electron-blocking layer, while SWNT functions as an efficient carrier dissociation and hole extraction layer in the band alignment (Fig. 10d). Combined with the PMMA layer as an effective barrier, high photovoltaic performance stability was achieved for SWNT–GO–PMMA based PSCs, where the PCE changed from 10.5% to 10% after 10 days, compared with that of the spiro-OMeTAD based PSC which dropped from 10.5% to 5.8%. The PSC with SWNT–GO–PMMA as the HTL showed a high PCE of 13.3% (Fig. 10e). When P3HT was in conjunction with MWCNTs and used as a HTL in a $CsPbI_2Br$ PSC, Wang *et al.* demonstrated that a conversion efficiency of 10.01% was achieved due to enhanced hole extraction and transport.[143] MWCNTs–P3HT composites also prevented moisture ingress, and ~85% of initial PCE was retained over 240 h under ambient conditions.

For composite HTL materials, the prevention of CNM aggregation in the polymer matrix is a key issue to create well-separated pathways for charge percolation in a specific direction at the nanoscale level. Thus, the functionalization of carbon nanomaterials with organic groups is a useful way to facilitate their homogeneous dispersion in polymer matrices. In 2016, Gatti *et al.* reported a P3HT [poly(3-hexylthiophene)] matrix doped with organic functionalized SWCNTs and rGO as the HTL in PSC devices.[88] To facilitate the dispersion of SWCNTs and rGO in the P3HT polymer matrix, *p*-methoxyphenyl substituents were introduced to form composite HTLs (Fig. 10f). Using 2 wt% SWCNT–PhOMe–P3HT and 4 wt% rGO–PhOMe–P3HT composites, the best PCEs of 11.6% and 10% for planar PSCs were achieved, and PCEs of 11% and 7.3% were retained after a 480 h endurance test, respectively (Fig. 10g and h). Moreover, after the endurance tests of over 3240 h, SWNT-

and rGO-doped PSCs showed an average PCE of 8.7% and 4.7% compared to the devices based on the un-doped polymer (PCE = 0). The increase in photovoltaic performances and stabilities was attributed to the improved interfacial contacts between the HTL and adjunct layers. In 2018, Gatti *et al.* further investigated the effect of five different substituent bonds (thienyl-type and alkyl-type) to rGO flakes on the morphology and structure of functionalized rGO–P3HT HTLs (Fig. 10i).[144] They demonstrated that the morphology of dispersed rGO flakes in a P3HT thin film could be tuned by tailoring the intermolecular interactions between two constituents in the composite. Table 3 summaries the device configurations and PV performances of PSCs using carbon–polymer composites as charge transport layers.

5. Conclusions and outlook

This review systematically summarized carbon materials–polymer composites that play various roles in nearly every component in PSC architectures, ranging from perovskite additives, electrodes, protective encapsulation to charge transporters. The composite structures were designed dependent on their roles in PSCs. For instance, as hole transport materials, carbon–polymer composites can modify the beneath perovskite layer for higher crystallinity and fewer traps or defects, alleviate energy-level gradients to improve open circuit voltage and increase the conductivity of the interlayer to facilitate hole extraction and transport.

Carbon–polymer composites demonstrated great potential to address the efficiency and stability issues of PSCs. Until now, among the carbon–polymer composite based devices, the highest PCE of 21.21% was reported in the one using graphene–Lewis base polymer composites as additives in perovskite.[123] This device retained 90% of its initial PCE after 480 h aging at ~35% relative humidity. Regarding the future research of carbon–polymer composite in PSCs, we propose the following prospects:

(i) Investigation of the transport mechanism of electrons and holes in carbon–polymer composites. Numerous studies have presented explanations of better photovoltaic performance from composite incorporation in terms of enhanced hole or electron transport and extraction. However, the charge transport kinetic process in composites was not investigated. Computational simulation can be conducted to analyse the carrier migration.

(ii) Characterization of the interface between carbon materials and polymers. Polymers were mixed with, coated on, infiltrated in or wrapped on carbon materials to form composites. The synergic effect of carbon and polymer has been confirmed to considerably improve its conductivity and thermal and mechanical properties. However, the interaction (*i.e.*, bonding method) between carbon materials and polymers as well as its influence on PSC devices need to attract more attention. This fundamental understanding benefits the specific design of composite materials in PSCs.

(iii) *In situ*/*operando* characterization to analyse the functions of carbon–polymer composites. *In situ* transmission electron microscopy, *in situ* X-ray diffraction analysis and other advanced analysis techniques should be used to directly observe perovskite crystallization or charge transport in the interlayer and interfaces of PSCs. The mechanism of composite modification should be explained better through such investigation.

List of abbreviations

PV	Photovoltaic
PSCs	Perovskite solar cells
PCE	Power conversion efficiency
$FAPbI_3$	Formamidinium lead triiodide
Spiro-OMeTAD	2,20,7,70-Tetrakis-(*N*,*N*-di-*p*-methoxyphenylamine)9,90-spirobifluorene
TCO	Transparent conductive oxide
ITO	Indium tin oxide
FTO	Fluorine tin oxide
CNMs	Carbon nanomaterials
rGO	Reduced graphene oxide
GO	Graphene oxide
CNTs	Carbon nanotubes
SWNTs	Single walled nanotubes
MWNTs	Multi-walled nanotubes
ETL	Electron transport layer
HTL	Hole transport later
ETM	Electron transport material
HTM	Hole transport material
P3HT	Poly(3-hexylthiophene)
TBP	4-*tert*-Butylpyridine
PCBM	[6,6]-Phenyl-C61-butyric acid methyl ester
PTEt	Poly(3-thiophene ethanol)
PMMA	Poly(methyl methacrylate)
PANI	Polyaniline
PEDOT	Poly(3,4-ethylenedioxythiophene)
PSSA	Poly(styrenesulfonic acid)
PP	Polypropylene
PS	Polystyrene
PC	Polycarbonate
PEN	Poly(ethylene-2,6-naphthalate)
CSCNT	Cross-stacked CNT
AgNW	Ag nanowire
GQDs	Graphene quantum dots
CQDs	Carbon quantum dots
CNDs	Carbon nanodots
GBs	Grain boundaries
PffBT4T-2OD	Poly[(5,6-difluoro-2,1,3-benzothiadiazol-4,7-diyl)-*alt*-(3,3‴-di(2-octyldodecyl)-2,2′;5′,2″;5″,2‴-quaterthiophen-5,5‴-diyl)]
PTFE	Polytetrafluoroethylene
PDMS	Poly(dimethylsiloxane)
EVOH	Poly(vinyl alcohol-*co*-ethylene)
PEDOT:PSS	Poly(3,4-ethylenedioxythiophene):poly(styrene sulfonate)
PTh	Polythiophene
P3HT	Poly(3-hexylthiophene)
PVP	Poly(*N*-vinylpyrrolidone)
PEI	Polyethylenimine
PTAA	Poly[bis(4-phenyl)(2,4,6-trimethylphenyl)amine]
PhOMe	*p*-Methoxyphenyl

Conflicts of interest

There are no conflicts to declare.

Acknowledgements

This material is based upon work supported by the U.S. Department of Energy's Office of Energy Efficiency and Renewable Energy (EERE) under the Solar Energy Technologies Office Award Number DE-EE0009525. The views expressed herein do not necessarily represent the views of the U.S. Department of Energy or the United States Government.

References

1 S. J. Zinkle and G. Was, *Acta Mater.*, 2013, **61**, 735–758.
2 G. J. Herbert, S. Iniyan, E. Sreevalsan and S. Rajapandian, *Renewable Sustainable Energy Rev.*, 2007, **11**, 1117–1145.
3 J. Zhang, J. Fan, B. Cheng, J. Yu and W. Ho, *Sol. RRL*, 2020, **4**, 2000502.
4 P. K. Nayak, S. Mahesh, H. J. Snaith and D. Cahen, *Nat. Rev. Mater.*, 2019, **4**, 269–285.
5 P. You, G. Tang and F. Yan, *Mater. Today Energy*, 2019, **11**, 128–158.
6 A. Kojima, K. Teshima, Y. Shirai and T. Miyasaka, *J. Am. Chem. Soc.*, 2009, **131**, 6050–6051.
7 F. Bella, *Electrochim. Acta*, 2015, **175**, 151–161.
8 M. M. Lee, J. Teuscher, T. Miyasaka, T. N. Murakami and H. J. Snaith, *Science*, 2012, **338**, 643–647.
9 H.-S. Kim, C.-R. Lee, J.-H. Im, K.-B. Lee, T. Moehl, A. Marchioro, S.-J. Moon, R. Humphry-Baker, J.-H. Yum and J. E. Moser, *Sci. Rep.*, 2012, **2**, 1–7.
10 N. NREL, Research-Cell Efficiencies, accessed April, 2022, **https://www.nrel.gov/pv/cell-efficiency.html**.
11 M. Kim, J. Jeong, H. Lu, T. K. Lee, F. T. Eickemeyer, Y. Liu, I. W. Choi, S. J. Choi, Y. Jo and H.-B. Kim, *Science*, 2022, **375**, 302–306.
12 W. E. Sha, X. Ren, L. Chen and W. C. Choy, *Appl. Phys. Lett.*, 2015, **106**, 221104.
13 D. Yang, R. Yang, K. Wang, C. Wu, X. Zhu, J. Feng, X. Ren, G. Fang, S. Priya and S. F. Liu, *Nat. Commun.*, 2018, **9**, 1–11.
14 Q. Luo, R. Wu, L. Ma, C. Wang, H. Liu, H. Lin, N. Wang, Y. Chen and Z. Guo, *Adv. Funct. Mater.*, 2021, **31**, 2004765.
15 J. Burschka, N. Pellet, S.-J. Moon, R. Humphry-Baker, P. Gao, M. K. Nazeeruddin and M. Grätzel, *Nature*, 2013, **499**, 316–319.
16 M. Liu, M. B. Johnston and H. J. Snaith, *Nature*, 2013, **501**, 395–398.
17 S. N. Habisreutinger, T. Leijtens, G. E. Eperon, S. D. Stranks, R. J. Nicholas and H. J. Snaith, *Nano Lett.*, 2014, **14**, 5561–5568.
18 V. Ferguson, S. R. P. Silva and W. Zhang, *Energy Environ. Mater.*, 2019, **2**, 107–118.
19 Y. Rong, Y. Hu, A. Mei, H. Tan, M. I. Saidaminov, S. I. Seok, M. D. McGehee, E. H. Sargent and H. Han, *Science*, 2018, **361**, eaat8235.
20 K. Domanski, J.-P. Correa-Baena, N. Mine, M. K. Nazeeruddin, A. Abate, M. Saliba, W. Tress, A. Hagfeldt and M. Grätzel, *ACS Nano*, 2016, **10**, 6306–6314.
21 H. Su, T. Wu, D. Cui, X. Lin, X. Luo, Y. Wang and L. Han, *Small Methods*, 2020, **4**, 2000507.
22 L. Wang, H. Zhou, J. Hu, B. Huang, M. Sun, B. Dong, G. Zheng, Y. Huang, Y. Chen and L. Li, *Science*, 2019, **363**, 265–270.
23 J.-P. Correa-Baena, M. Saliba, T. Buonassisi, M. Grätzel, A. Abate, W. Tress and A. Hagfeldt, *Science*, 2017, **358**, 739–744.
24 Z. Ku, Y. Rong, M. Xu, T. Liu and H. Han, *Sci. Rep.*, 2013, **3**, 1–5.
25 N. Arora, M. I. Dar, A. Hinderhofer, N. Pellet, F. Schreiber, S. M. Zakeeruddin and M. Grätzel, *Science*, 2017, **358**, 768–771.
26 M. Li, W. W. Zuo, Q. Wang, K. L. Wang, M. P. Zhuo, H. Köbler, C. E. Halbig, S. Eigler, Y. G. Yang and X. Y. Gao, *Adv. Energy Mater.*, 2020, **10**, 1902653.
27 X. Li, T. Tong, Q. Wu, S. Guo, Q. Song, J. Han and Z. Huang, *Adv. Funct. Mater.*, 2018, **28**, 1800475.
28 A. P. Litvin, X. Zhang, K. Berwick, A. V. Fedorov, W. Zheng and A. V. Baranov, *Renewable Sustainable Energy Rev.*, 2020, **124**, 109774.
29 N. E. Safie, M. A. Azam, M. F. Aziz and M. Ismail, *Int. J. Energy Res.*, 2021, **45**, 1347–1374.
30 M. Hadadian, J.-H. Smått and J.-P. Correa-Baena, *Energy Environ. Sci.*, 2020, **13**, 1377–1407.
31 K. Moore and W. Wei, *Nano Mater. Sci.*, 2021, **3**, 276–290.
32 F. Bonaccorso, A. Bartolotta, J. N. Coleman and C. Backes, *Adv. Mater.*, 2016, **28**, 6136–6166.
33 F. Meng, A. Liu, L. Gao, J. Cao, Y. Yan, N. Wang, M. Fan, G. Wei and T. Ma, *J. Mater. Chem. A*, 2019, **7**, 8690–8699.
34 Y. Gao, *Nanoscale Res. Lett.*, 2017, **12**, 1–17.
35 M. Batmunkh, C. J. Shearer, M. J. Biggs and J. G. Shapter, *J. Mater. Chem. A*, 2015, **3**, 9020–9031.
36 Y. Bai, X. Meng and S. Yang, *Adv. Energy Mater.*, 2018, **8**, 1701883.
37 F. Wang, Y. Cao, C. Chen, Q. Chen, X. Wu, X. Li, T. Qin and W. Huang, *Adv. Funct. Mater.*, 2018, **28**, 1803753.
38 V. D'innocenzo, G. Grancini, M. J. Alcocer, A. R. S. Kandada, S. D. Stranks, M. M. Lee, G. Lanzani, H. J. Snaith and A. Petrozza, *Nat. Commun.*, 2014, **5**, 1–6.
39 S. Kim, H. S. Lee, J. M. Kim, S. W. Seo, J. H. Kim, C. W. Jang and S.-H. Choi, *J. Alloys Compd.*, 2018, **744**, 404–411.
40 K. Petridis, G. Kakavelakis, M. M. Stylianakis and E. Kymakis, *Chem.–Asian J.*, 2018, **13**, 240–249.
41 P.-C. Hsu, D. Kong, S. Wang, H. Wang, A. J. Welch, H. Wu and Y. Cui, *J. Am. Chem. Soc.*, 2014, **136**, 10593–10596.
42 S. De, P. E. Lyons, S. Sorel, E. M. Doherty, P. J. King, W. J. Blau, P. N. Nirmalraj, J. J. Boland, V. Scardaci and J. Joimel, *ACS Nano*, 2009, **3**, 714–720.
43 H.-Z. Geng, K. K. Kim, K. P. So, Y. S. Lee, Y. Chang and Y. H. Lee, *J. Am. Chem. Soc.*, 2007, **129**, 7758–7759.
44 T. Minami, *Thin Solid Films*, 2008, **516**, 5822–5828.
45 S. He, L. Qiu, D.-Y. Son, Z. Liu, E. J. Juarez-Perez, L. K. Ono, C. Stecker and Y. Qi, *ACS Energy Lett.*, 2019, **4**, 2032–2039.

46 W.-J. Yin, T. Shi and Y. Yan, *Appl. Phys. Lett.*, 2014, **104**, 063903.
47 N. Aristidou, I. Sanchez-Molina, T. Chotchuangchutchaval, M. Brown, L. Martinez, T. Rath and S. A. Haque, *Angew. Chem.*, 2015, **127**, 8326–8330.
48 M. Grätzel, *Nat. Mater.*, 2014, **13**, 838–842.
49 M. A. Green, A. Ho-Baillie and H. J. Snaith, *Nat. Photonics*, 2014, **8**, 506–514.
50 R. Wang, M. Mujahid, Y. Duan, Z. K. Wang, J. Xue and Y. Yang, *Adv. Funct. Mater.*, 2019, **29**, 1808843.
51 J. Niu, D. Yang, X. Ren, Z. Yang, Y. Liu, X. Zhu, W. Zhao and S. F. Liu, *Org. Electron.*, 2017, **48**, 165–171.
52 M. Jørgensen, K. Norrman and F. C. Krebs, *Sol. Energy Mater. Sol. Cells*, 2008, **92**, 686–714.
53 D. B. Kim, J. C. Yu, Y. S. Nam, D. W. Kim, E. D. Jung, S. Y. Lee, S. Lee, J. H. Park, A.-Y. Lee and B. R. Lee, *J. Mater. Chem. C*, 2016, **4**, 8161–8165.
54 Z. Wu, S. Bai, J. Xiang, Z. Yuan, Y. Yang, W. Cui, X. Gao, Z. Liu, Y. Jin and B. Sun, *Nanoscale*, 2014, **6**, 10505–10510.
55 E. Jokar, Z. Y. Huang, S. Narra, C. Y. Wang, V. Kattoor, C. C. Chung and E. W. G. Diau, *Adv. Energy Mater.*, 2018, **8**, 1701640.
56 M. Z. Iqbal, J. U. Nabi, S. Siddique, H. T. A. Awan, S. S. Haider and M. Sulman, *Int. J. Energy Res.*, 2020, **44**, 1464–1487.
57 J.-S. Yeo, R. Kang, S. Lee, Y.-J. Jeon, N. Myoung, C.-L. Lee, D.-Y. Kim, J.-M. Yun, Y.-H. Seo and S.-S. Kim, *Nano Energy*, 2015, **12**, 96–104.
58 P. You, Z. Liu, Q. Tai, S. Liu and F. Yan, *Adv. Mater.*, 2015, **27**, 3632–3638.
59 Z. Zhu, J. Ma, Z. Wang, C. Mu, Z. Fan, L. Du, Y. Bai, L. Fan, H. Yan and D. L. Phillips, *J. Am. Chem. Soc.*, 2014, **136**, 3760–3763.
60 Q. Luo, H. Ma, Q. Hou, Y. Li, J. Ren, X. Dai, Z. Yao, Y. Zhou, L. Xiang and H. Du, *Adv. Funct. Mater.*, 2018, **28**, 1706777.
61 D. Bogachuk, S. Zouhair, K. Wojciechowski, B. Yang, V. Babu, L. Wagner, B. Xu, J. Lim, S. Mastroianni and H. Pettersson, *Energy Environ. Sci.*, 2020, **13**, 3880–3916.
62 S. Wang, Z. Zhang, Z. Tang, C. Su, W. Huang, Y. Li and G. Xing, *Nano Energy*, 2021, **82**, 105712.
63 D. M. Jones, J. Hidalgo, Y. An, C. Evans, J. Vagott and J.-P. Correa-Baena, *J. Mater. Chem. C*, 2021, 12509–12522.
64 W. Hou, Y. Xiao, G. Han and J.-Y. Lin, *Polymers*, 2019, **11**, 143.
65 W. Chee, H. Lim, N. Huang and I. Harrison, *RSC Adv.*, 2015, **5**, 68014–68051.
66 K. S. Novoselov, A. K. Geim, S. V. Morozov, D.-e. Jiang, Y. Zhang, S. V. Dubonos, I. V. Grigorieva and A. A. Firsov, *Science*, 2004, **306**, 666–669.
67 Z. Chen, Y. Qi, X. Chen, Y. Zhang and Z. Liu, *Adv. Mater.*, 2019, **31**, 1803639.
68 C. Lee, X. Wei, J. W. Kysar and J. Hone, *Science*, 2008, **321**, 385–388.
69 K. I. Bolotin, K. J. Sikes, Z. Jiang, M. Klima, G. Fudenberg, J. Hone, P. Kim and H. Stormer, *Solid State Commun.*, 2008, **146**, 351–355.
70 A. A. Balandin, S. Ghosh, W. Bao, I. Calizo, D. Teweldebrhan, F. Miao and C. N. Lau, *Nano Lett.*, 2008, **8**, 902–907.
71 F. Bonaccorso, Z. Sun, T. Hasan and A. Ferrari, *Nat. Photonics*, 2010, **4**, 611–622.
72 S. Javaid, C. W. Myung, S. Pourasad, B. Rakshit, K. S. Kim and G. Lee, *J. Mater. Chem. A*, 2018, **6**, 18635–18640.
73 Y. Zhu, S. Murali, W. Cai, X. Li, J. W. Suk, J. R. Potts and R. S. Ruoff, *Adv. Mater.*, 2010, **22**, 3906–3924.
74 O. C. Compton and S. T. Nguyen, *Small*, 2010, **6**, 711–723.
75 R. Tarcan, O. Todor-Boer, I. Petrovai, C. Leordean, S. Astilean and I. Botiz, *J. Mater. Chem. C*, 2020, **8**, 1198–1224.
76 S. Iijima, *Nature*, 1991, **354**, 56–58.
77 G. Mittal, V. Dhand, K. Y. Rhee, S.-J. Park and W. R. Lee, *J. Ind. Eng. Chem.*, 2015, **21**, 11–25.
78 C. Xia, S. Zhu, T. Feng, M. Yang and B. Yang, *Adv. Sci.*, 2019, **6**, 1901316.
79 Z. Kang and S.-T. Lee, *Nanoscale*, 2019, **11**, 19214–19224.
80 Q. Guo, F. Yuan, B. Zhang, S. Zhou, J. Zhang, Y. Bai, L. Fan, T. Hayat, A. Alsaedi and Z. a. Tan, *Nanoscale*, 2019, **11**, 115–124.
81 Z. Wang, F. Yuan, W. Sun, H. Shi, T. Hayat, A. Alsaedi, L. Fan and Z. a. Tan, *Adv. Opt. Mater.*, 2019, **7**, 1901299.
82 X. Guo, B. Zhao, K. Xu, S. Yang, Z. Liu, Y. Han, J. Xu, D. Xu, Z. Tan and S. Liu, *Small*, 2021, **17**, 2102272.
83 A. Cayuela, M. Soriano, C. Carrillo-Carrión and M. Valcárcel, *Chem. Commun.*, 2016, **52**, 1311–1326.
84 G. S. Han, J. S. Yoo, F. Yu, M. L. Duff, B. K. Kang and J.-K. Lee, *J. Mater. Chem. A*, 2017, **5**, 14733–14740.
85 X. Zheng, H. Chen, Z. Wei, Y. Yang, H. Lin and S. Yang, *Frontiers of Optoelectronics*, 2016, **9**, 71–80.
86 A. Giuri, S. Masi, S. Colella, A. Listorti, A. Rizzo, A. Kovtun, S. Dell'Elce, A. Liscio and C. Esposito Corcione, *Polym. Eng. Sci.*, 2017, **57**, 546–552.
87 A. Kumar, K. Sharma and A. R. Dixit, *Carbon Letters*, 2021, **31**, 149–165.
88 T. Gatti, S. Casaluci, M. Prato, M. Salerno, F. Di Stasio, A. Ansaldo, E. Menna, A. Di Carlo and F. Bonaccorso, *Adv. Funct. Mater.*, 2016, **26**, 7443–7453.
89 J. W. Jung, S. H. Son and J. Choi, *Polymers*, 2021, **13**, 1281.
90 F. Barroso-Bujans, S. Cerveny, R. Verdejo, J. d. del Val, J. M. Alberdi, A. Alegría and J. Colmenero, *Carbon*, 2010, **48**, 1079–1087.
91 H. Mohseni, M. Dehghanipour, N. Dehghan, F. Tamaddon, M. Ahmadi, M. Sabet and A. Behjat, *Sol. Energy*, 2021, **213**, 59–66.
92 S. W. Tong, J. Balapanuru, D. Fu and K. P. Loh, *ACS Appl. Mater. Interfaces*, 2016, **8**, 29496–29503.
93 S. Cogal, L. Calio, G. C. Cogal, M. Salado, S. Kazim, L. Oksuz, S. Ahmad and A. U. Oksuz, *Polym. Bull.*, 2018, **75**, 4531–4545.
94 P. Pötschke, A. R. Bhattacharyya and A. Janke, *Eur. Polym. J.*, 2004, **40**, 137–148.
95 J. Y. Kim and S. H. Kim, *J. Polym. Sci., Part B: Polym. Phys.*, 2006, **44**, 1062–1071.
96 B. Shen, W. Zhai, M. Tao, D. Lu and W. Zheng, *Compos. Sci. Technol.*, 2013, **86**, 109–116.

97 E. Nilsson, H. Oxfall, W. Wandelt, R. Rychwalski and B. Hagström, *J. Appl. Polym. Sci.*, 2013, **130**, 2579–2587.
98 Y. Zhou, X. Yin, Q. Luo, X. Zhao, D. Zhou, J. Han, F. Hao, M. Tai, J. Li and P. Liu, *ACS Appl. Mater. Interfaces*, 2018, **10**, 31384–31393.
99 F. Wang, M. Endo, S. Mouri, Y. Miyauchi, Y. Ohno, A. Wakamiya, Y. Murata and K. Matsuda, *Nanoscale*, 2016, **8**, 11882–11888.
100 H. Dong, Z. Wu, Y. Jiang, W. Liu, X. Li, B. Jiao, W. Abbas and X. Hou, *ACS Appl. Mater. Interfaces*, 2016, **8**, 31212–31221.
101 S. Qin, C. Chen, M. Cui, A. Zhang, H. Zhao and L. Wang, *RSC Adv.*, 2017, **7**, 3003–3011.
102 J. Wang, F. Song, Y. Ding and M. Shao, *Mater. Des.*, 2020, **195**, 109073.
103 P. Govindaraj, B. Fox, P. Aitchison and N. Hameed, *Ind. Eng. Chem. Res.*, 2019, **58**, 17106–17129.
104 R. Bauld, D.-Y. W. Choi, P. Bazylewski, R. Divigalpitiya and G. Fanchini, *J. Mater. Chem. C*, 2018, **6**, 2901–2914.
105 W. Park, J. Hu, L. A. Jauregui, X. Ruan and Y. P. Chen, *Appl. Phys. Lett.*, 2014, **104**, 113101.
106 H. Wang, Q. Hao, X. Yang, L. Lu and X. Wang, *Electrochem. Commun.*, 2009, **11**, 1158–1161.
107 S. Mabrouk, B. Bahrami, H. Elbohy, K. M. Reza, A. Gurung, M. Liang, F. Wu, M. Wang, S. Yang and Q. Qiao, *InfoMat*, 2020, **2**, 928–941.
108 Q. Li, Y. Guo, W. Li, S. Qiu, C. Zhu, X. Wei, M. Chen, C. Liu, S. Liao and Y. Gong, *Chem. Mater.*, 2014, **26**, 4459–4465.
109 Y.-F. Zhang, Y.-J. Ren and S.-L. Bai, *Int. J. Heat Mass Transfer*, 2018, **118**, 510–517.
110 A. Yu, P. Ramesh, M. E. Itkis, E. Bekyarova and R. C. Haddon, *J. Phys. Chem. C*, 2007, **111**, 7565–7569.
111 W. Guo and G. Chen, *J. Appl. Polym. Sci.*, 2014, **131**, 40565.
112 K. M. Shahil and A. A. Balandin, *Nano Lett.*, 2012, **12**, 861–867.
113 M. A. García and J. Balenzategui, *Renewable Energy*, 2004, **29**, 1997–2010.
114 X. Ji, Y. Xu, W. Zhang, L. Cui and J. Liu, *Composites, Part A*, 2016, **87**, 29–45.
115 D. Qian, E. C. Dickey, R. Andrews and T. Rantell, *Appl. Phys. Lett.*, 2000, **76**, 2868–2870.
116 Q. Zhao, Y. Shen, M. Ji, L. Zhang, T. Jiang and C. Li, *J. Ind. Eng. Chem.*, 2014, **20**, 544–548.
117 N. Rajamanickam, S. Kumari, V. K. Vendra, B. W. Lavery, J. Spurgeon, T. Druffel and M. K. Sunkara, *Nanotechnology*, 2016, **27**, 235404.
118 N. Ahn, I. Jeon, J. Yoon, E. I. Kauppinen, Y. Matsuo, S. Maruyama and M. Choi, *J. Mater. Chem. A*, 2018, **6**, 1382–1389.
119 H. W. Lee, Y. Yoon, S. Park, J. H. Oh, S. Hong, L. S. Liyanage, H. Wang, S. Morishita, N. Patil and Y. J. Park, *Nat. Commun.*, 2011, **2**, 1–8.
120 R. Sarvari, S. Agbolaghi and B. Massoumi, *Opt. Mater.*, 2019, **92**, 81–86.
121 C. Eames, J. M. Frost, P. R. Barnes, B. C. O'regan, A. Walsh and M. S. Islam, *Nat. Commun.*, 2015, **6**, 1–8.
122 Y. Shao, Y. Fang, T. Li, Q. Wang, Q. Dong, Y. Deng, Y. Yuan, H. Wei, M. Wang and A. Gruverman, *Energy Environ. Sci.*, 2016, **9**, 1752–1759.
123 Q. Lou, G. Lou, R. Peng, Z. Liu, W. Wang, M. Ji, C. Chen, X. Zhang, C. Liu and Z. Ge, *ACS Appl. Energy Mater.*, 2021, **4**, 3928–3936.
124 X. Xu, Q. Chen, Z. Hong, H. Zhou, Z. Liu, W.-H. Chang, P. Sun, H. Chen, N. D. Marco and M. Wang, *Nano Lett.*, 2015, **15**, 6514–6520.
125 Y. Rong, Y. Hu, A. Mei, H. Tan, M. I. Saidaminov, S. I. Seok, M. D. McGehee, E. H. Sargent and H. Han, *Science*, 2018, **361**, eaat8235.
126 A. Guerrero, J. You, C. Aranda, Y. S. Kang, G. Garcia-Belmonte, H. Zhou, J. Bisquert and Y. Yang, *ACS Nano*, 2016, **10**, 218–224.
127 J. H. Jang, B.-J. Kim, J.-h. Kim, E. Han, E. Y. Choi, C. H. Ji, K.-T. Kim, J. Kim and N. Park, *ACS Omega*, 2019, **4**, 9211–9218.
128 J. Xu, K. Wang, S.-Z. Zu, B.-H. Han and Z. Wei, *ACS Nano*, 2010, **4**, 5019–5026.
129 Y.-C. Yong, X.-C. Dong, M. B. Chan-Park, H. Song and P. Chen, *ACS Nano*, 2012, **6**, 2394–2400.
130 J. Yang, B. D. Siempelkamp, E. Mosconi, F. De Angelis and T. L. Kelly, *Chem. Mater.*, 2015, **27**, 4229–4236.
131 D.-Y. Lee, S.-I. Na and S.-S. Kim, *Nanoscale*, 2016, **8**, 1513–1522.
132 C. Redondo-Obispo, T. S. Ripolles, S. Cortijo-Campos, A. L. Alvarez, E. Climent-Pascual, A. de Andrés and C. Coya, *Mater. Des.*, 2020, **191**, 108587.
133 Q.-Q. Chu, B. Ding, J. Peng, H. Shen, X. Li, Y. Liu, C.-X. Li, C.-J. Li, G.-J. Yang and T. P. White, *J. Mater. Sci. Technol.*, 2019, **35**, 987–993.
134 J. Ye, X. Li, J. Zhao, X. Mei and Q. Li, *RSC Adv.*, 2016, **6**, 36356–36361.
135 J. C. Yu, J. A. Hong, E. D. Jung, D. B. Kim, S.-M. Baek, S. Lee, S. Cho, S. S. Park, K. J. Choi and M. H. Song, *Sci. Rep.*, 2018, **8**, 1–9.
136 H. Guo, X. Huang, B. Pu, J. Yang, H. Chen, Y. Zhou, J. Yang, Y. Li, Z. Wang and X. Niu, *RSC Adv.*, 2017, **7**, 50410–50419.
137 S.-P. Cho, G. Han, Y.-H. Seo, Y.-J. Noh, J.-Y. Sohn, I.-T. Hwang, J. Shin, C.-H. Jung and S.-I. Na, *Compos. Sci. Technol.*, 2021, **201**, 108548.
138 J. S. Cho, W. Jang, S. C. Mun, M. Yi, J. H. Park and D. H. Wang, *Carbon*, 2018, **139**, 564–571.
139 W. Li, N. Cheng, Y. Cao, Z. Zhao, Z. Xiao, W. Zi and Z. Sun, *Org. Electron.*, 2020, **78**, 105575.
140 Z. Li, C. Liu, X. Zhang, J. Guo, H. Cui, L. Shen, Y. Bi and W. Guo, *Mater. Today Energy*, 2019, **12**, 161–167.
141 S. N. Habisreutinger, T. Leijtens, G. E. Eperon, S. D. Stranks, R. J. Nicholas and H. J. Snaith, *J. Phys. Chem. Lett.*, 2014, **5**, 4207–4212.
142 S. N. Habisreutinger, B. Wenger, H. J. Snaith and R. J. Nicholas, *ACS Energy Lett.*, 2017, **2**, 622–628.
143 G. Wang, J. Liu, K. Chen, R. Pathak, A. Gurung and Q. Qiao, *J. Colloid Interface Sci.*, 2019, **555**, 180–186.
144 T. Gatti, F. Lamberti, P. Topolovsek, M. Abdu-Aguye, R. Sorrentino, L. Perino, M. Salerno, L. Girardi, C. Marega and G. A. Rizzi, *Sol. RRL*, 2018, **2**, 1800013.

